Langtaosha (LTS) Preprint doi: https://doi.org/10.65215/LTSpreprints.2026.11.11.000383. This version posted November 11, 2026. The copyright holder for this preprint (which was not certified by peer review) is the author/funder. Creative Commons license: CC Attribution-NonCommercial-NoDerivatives 4.0 https://creativecommons.org/licenses/by-nc-nd/4.0

Evolution and structural plasticity of microvilli

Silin Zhang[1]†, Fang Kong[1]†, Jiaxin Tan[1]†, Yang Shen[1], Tianwei Zhao[1], Shanjin Huang[1], Chuangye Yan[1]*

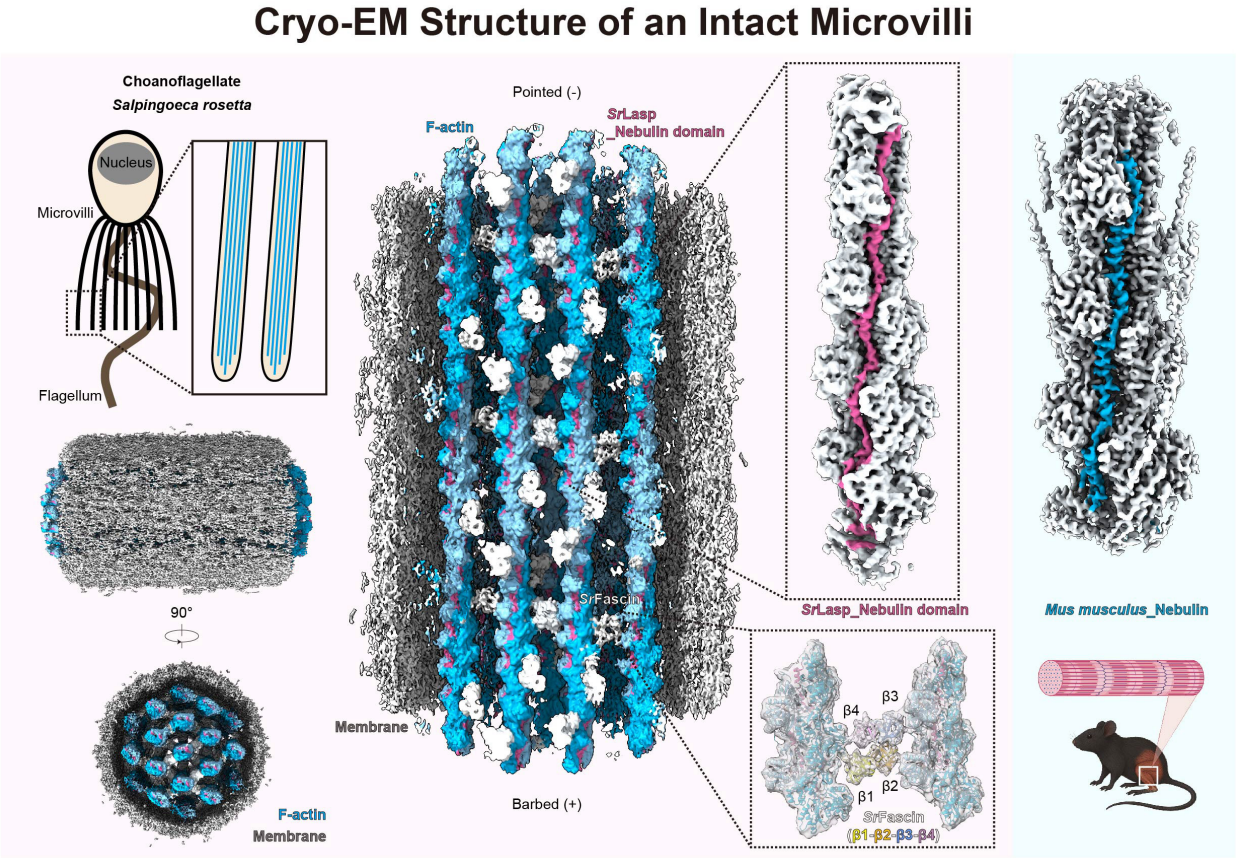
[1]Beijing Frontier Research Center for Biological Structure, Beijing Advanced Innovation Center for Structural Biology, State Key Laboratory of Membrane Biology, Tsinghua-Peking Joint Center for Life Sciences, School of Life Sciences, Tsinghua University, Beijing 100084, China.

†These authors contributed equally to this work.

*Correspondence: yancy2019@tsinghua.edu.cn (C.Y.).

Langtaosha (LTS) Preprint doi: https://doi.org/10.65215/LTSpreprints.2026.11.11.000383. This version posted November 11, 2026. The copyright holder for this preprint (which was not certified by peer review) is the author/funder. Creative Commons license: CC Attribution-NonCommercial-NoDerivatives 4.0 https://creativecommons.org/licenses/by-nc-nd/4.0

Graphical abstract



In brief

Cryo-EM analysis of choanoflagellate microvilli reveals an ancestral Nebulin-family protein, Lasp, that binds actin through a mechanism conserved in vertebrate Nebulin, and a Fascin-mediated crosslinking pattern that accommodates the helical geometry of actin filaments within hexagonal bundles, providing insights into the evolution and structural organization of microvilli.

Highlights

- *In situ* cryo-EM reveals the molecular architecture of choanoflagellate microvilli
- An ancestral Lasp shares a conserved actin-binding mechanism with vertebrate Nebulin
- Fascin adopts alternative binding patterns to accommodate actin helical geometry
- *Sr*Lasp stabilizes and bundles actin filaments through distinct structural domains

Langtaosha (LTS) Preprint doi: https://doi.org/10.65215/LTSpreprints.2026.11.11.000383. This version posted November 11, 2026. The copyright holder for this preprint (which was not certified by peer review) is the author/funder. Creative Commons license: CC Attribution-NonCommercial-NoDerivatives 4.0 https://creativecommons.org/licenses/by-nc-nd/4.0

SUMMARY

Actin-based protrusions shape cellular morphology and mediate environmental sensing, yet the evolutionary timeline and structural principles governing their organization are not fully understood. Here, we investigate the unicellular frontier of metazoan multicellularity by resolving the native architecture of microvilli in the choanoflagellate *Salpingoeca rosetta* using *in situ* cryo-electron tomography and single-particle cryo-electron microscopy. We discover that these premetazoan microvilli are sustained by a highly ordered, hexagonal actin array cross-bridged by *Sr*Fascin and decorated by *Sr*Lasp,an ancestral member of the Nebulin-family protein. Structural analysis reveals that *Sr*Lasp engages F-actin through a binding mechanism conserved in vertebrate skeletal muscle Nebulin, suggesting that this mode of actin regulation predates the emergenc of animals. Beyond this profound evolutionary conservation, the microvillar cytoskeleton exhibits remarkable structural plasticity to accommodate geometric constraints. Fascin cross-bridges adjacent filaments within the 7-filament core through discrete "skip-or-flip" shifts in crossbridging register, accommodating the intrinsic helical mismatch between neighboring actin filaments. Together, these findings delineate a primordial actin-organizing module for microvillar architecture and illuminate the evolutionary origins of Nebulin-family actin regulation before the emergence of animals.

Langtaosha (LTS) Preprint doi: https://doi.org/10.65215/LTSpreprints.2026.11.11.000383. This version posted November 11, 2026. The copyright holder for this preprint (which was not certified by peer review) is the author/funder. Creative Commons license: CC Attribution-NonCommercial-NoDerivatives 4.0 https://creativecommons.org/licenses/by-nc-nd/4.0

INTRODUCTION

Actin-based protrusions are fundamental cellular structures that enable cells to sense, interact with, and respond to their environment. In animals, diverse actin-based protrusions, such as lamellipodia, filopodia, and invadopodia, support a wide range of cellular functions, including migration, environmental sensing, and tissue invasion[1-3], and microvilli facilitate absorptive and sensory functions[4] (Figures S1A and S1B). Despite their distinct morphologies and functions, these protrusions are all built upon specialized actin cytoskeletal architectures, ranging from branched actin networks in lamellipodia to tightly packed parallel actin bundles in filopodia and microvilli[1-4]. Although numerous actin-binding proteins have been implicated in their assembly and regulation, high-resolution *in situ* structural information remains limited, leaving the molecular principles governing actin organization within native cellular environments poorly understood.

Among actin-based protrusions, microvilli represent one of the most highly ordered actin assemblies, with densely packed parallel actin filaments arranged in a stereotyped architecture[5]. These features make microvilli an ideal system for investigating how actin filaments are organized within their native cellular context. Previous structural studies of isolated brush borders have provided valuable insights into microvillar architecture, but sample preparation can partially disrupt the fragile actin core and compromise its native organization[6]. More recently, *in situ* cryo-electron tomography (cryo-ET) has begun to reveal microvillar organization within intact tissues[7]. However, the resolution currently achievable of cryo-ET *in situ* remains insufficient to resolve many actin-associated proteins and their interactions with F-actin. As a result, current molecular models of microvillar organization largely rely on integrating electron microscopy (EM), diffraction measurements, and atomic structures of individual components[8]. The molecular architecture of native microvillar actin bundles therefore remains incompletely understood.

Langtaosha (LTS) Preprint doi: https://doi.org/10.65215/LTSpreprints.2026.11.11.000383. This version posted November 11, 2026. The copyright holder for this preprint (which was not certified by peer review) is the author/funder. Creative Commons license: CC Attribution-NonCommercial-NoDerivatives 4.0 https://creativecommons.org/licenses/by-nc-nd/4.0

Recent advances in cryo-EM have enabled the identification of endogenous proteins directly within native cellular structures, allowing molecular functions to be inferred from their structural context[9-11]. To harness these advances, we turned to the evolutionary history of actin-based protrusions in search of a model system that combines native structural preservation with the potential for high-resolution cryo-EM analysis (Figure 1A). Within Amorphea, a major eukaryotic supergroup encompassing animals and amoeboid lineages, actin-dependent crawling mediated by filopodia- and lamellipodia-like protrusions is thought to be an ancient mode of cell motility[12,13]. Within Filozoa, which encompasses filastereans[14], choanoflagellates, and metazoans, actin-supported projections exhibit increasingly specialized and stereotyped architectures[15]. Choanoflagellates, the closest living unicellular relatives of animals[16], possess a characteristic collar of microvilli surrounding a single flagellum, which generates water flow and captures bacterial prey for feeding (Figure 1B)[17]. This collar is thought to share deep evolutionary homology with animal microvilli (Figure S1B)[4,12]. Their small cell size, highly ordered actin bundles, and close evolutionary relationship to animals make choanoflagellates an ideal system for high-resolution structural analysis of the evolutionary origins of microvillar actin organization.

Here, we combine cryo-ET and single-particle cryo-EM to resolve the molecular architecture of microvilli in the choanoflagellate *Salpingoeca rosetta* (*S. rosetta*). We identify a previously uncharacterized Nebulin-family protein that binds microvillar actin filaments through a conserved Nebulin-like interface and characterize its structural and biochemical properties. We further resolve the native architecture of a Fascin-crosslinked actin bundles, revealing how Fascin accommodates the geometric constraints of filament packing. Together, these findings establish

Langtaosha (LTS) Preprint doi: https://doi.org/10.65215/LTSpreprints.2026.11.11.000383. This version posted November 11, 2026. The copyright holder for this preprint (which was not certified by peer review) is the author/funder. Creative Commons license: CC Attribution-NonCommercial-NoDerivatives 4.0 https://creativecommons.org/licenses/by-nc-nd/4.0

that a conserved mode of Nebulin-family actin recognition predates the emergence of animals, providing a structural framework for understanding the evolutionary origins of microvillar actin organization and muscle thin-filament architecture.

Langtaosha (LTS) Preprint doi: https://doi.org/10.65215/LTSpreprints.2026.11.11.000383. This version posted November 11, 2026. The copyright holder for this preprint (which was not certified by peer review) is the author/funder. Creative Commons license: CC Attribution-NonCommercial-NoDerivatives 4.0 https://creativecommons.org/licenses/by-nc-nd/4.0

RESULTS

A Nebulin-family protein associates with microvillar actin filaments in *S. rosetta*

To enable structural analysis of native actin-based protrusions, we established cryo-EM imaging of the choanoflagellate *S. rosetta*, whose collar of microvilli provides a highly ordered actin-based architecture (Figures 1B and 1C). We optimized culture conditions to enrich for isolated cells with elongated microvilli while minimizing bacterial contamination. Under starvation conditions, cells adopted a more elongated morphology, rendering the microvillar collar readily visible (Figures S2A and S2B; Movies S1 and S2). Cryo-EM micrographs also revealed well-preserved flagella and neighboring microvilli (Figure 1C). Individual microvilli remained intact along their entire length, from their base at the cell surface to the distal tip (Figures 1C and 1D). The underlying F-actin bundles remained continuous and highly ordered, exhibiting the characteristic periodic pattern of bundled actin filaments. Together, the preservation of intact microvilli and their abundant, repetitive actin architecture establish *S. rosetta* as an ideal system for *in situ* structural analysis of microvilli.

Using single-particle cryo-EM, we obtained a 3.16 Å reconstruction of an individual microvillar actin filament (Figures S3A-S3C). Unexpectedly, the reconstruction revealed additional ribbon-like densities extending along both inner helical grooves of the actin filament (Figure 1E). None of the known microvillar actin-associated proteins, including Fascin, Plastin, Villin, Espin, or Myosins, could be attributed to this density. Strikingly, its location and morphology closely resembled Nebulin densities recently resolved *in situ* along mouse skeletal muscle thin filaments[18,19].

Langtaosha (LTS) Preprint doi: https://doi.org/10.65215/LTSpreprints.2026.11.11.000383. This version posted November 11, 2026. The copyright holder for this preprint (which was not certified by peer review) is the author/funder. Creative Commons license: CC Attribution-NonCommercial-NoDerivatives 4.0 https://creativecommons.org/licenses/by-nc-nd/4.0

This raised the question of whether a Nebulin-family protein might exist in choanoflagellates. To identify the source of this density, we searched the *S. rosetta* proteome for Nebulin-family proteins. Initial searches using mouse Nebulin failed to identify convincing candidates, potentially due to its extreme size and highly repetitive architecture. We therefore examined the evolutionary relationships of Nebulin-family proteins across Holozoa (Figures S4A and S4B). Phylogenetic analysis recovered four Nebulin-family clades—Lasp, Nebulin, Nebulette, and N-RAP[20,21]. Whereas giant Nebulin proteins were restricted to vertebrates, Lasp homologs were conserved throughout Filozoa, including filastereans, choanoflagellates, and metazoans, suggesting that Lasp represents an evolutionarily ancient branch of the Nebulin family. Guided by this evolutionary framework, we used mouse Lasp-1 (Q543N3), the smallest member of the Nebulin family, as a BLAST query and identified a single candidate in *S. rosetta*, F2UDL6 (Figure S5A). F2UDL6 clustered robustly within the Lasp clade (Figure S4B) and exhibited the characteristic LIM-Nebulin-SH3 domain architecture (hereafter referred to as *Sr*Lasp) (Figure 1F).

There are two Nebulin repeats in *Sr*Lasp (Figure 1F). However, sequence conservation analysis suggested that Nebulin-1 more closely resembles canonical Nebulin-family actin-binding repeats, whereas Nebulin-2, despite retaining the characteristic -SxxxYx- motif, is substantially diverged at other conserved positions (Figure S5B). Consistent with these sequence features, only Nebulin-1 could be reliably fitted into the cryo-EM density, supporting the assignment of the previously unassigned actin-associated density to *Sr*Lasp (Figures 1F and 1G).

Structural basis of F-actin recognition by *Sr*Lasp

Langtaosha (LTS) Preprint doi: https://doi.org/10.65215/LTSpreprints.2026.11.11.000383. This version posted November 11, 2026. The copyright holder for this preprint (which was not certified by peer review) is the author/funder. Creative Commons license: CC Attribution-NonCommercial-NoDerivatives 4.0 https://creativecommons.org/licenses/by-nc-nd/4.0

To define the molecular basis of *Sr*Lasp–actin recognition, we analyzed the refined atomic model derived from the 3.16 Å reconstruction (Figure 2A). *Sr*Lasp binds within the inner helical groove of F-actin, extending across four consecutive actin subunits along the filament. The Nebulin repeat adopts an extended helix-linker-helix architecture, with its N terminus oriented toward the pointed (-) end and its C terminus toward the barbed (+) end of the actin filament (Figures 2A and 2B).

Both α-helices participate in actin recognition (Figure 2B). The N-terminal helix (Helix-1) establishes an extensive network of hydrogen bonds and electrostatic interactions with F-actin. Thr69, Asp73, and Glu76 contact actin subunit i+3, whereas Gln70 and Lys81 interact with subunit i+2. Pro75 and Arg79 establish additional contacts with subunit i+1. The linker and C-terminal helix (Helix-2) contribute further interactions, with Gln87 contacting subunit i+1, Tyr92 contacting subunit i+2, and Lys94 and Gln95 contacting subunit i. In addition, Tyr96 forms a hydrophobic interaction with Ile76 of actin subunit i+3. Together, these interactions form an extended binding interface spanning multiple actin subunits rather than a single dominant interaction hotspot. Notably, many residues at the *Sr*Lasp-actin interface are conserved across Nebulin-family repeats, including those within the characteristic DTPE-containing segment and the canonical SxxxYx motif (Figure 2C).

To assess the contribution of the two Nebulin repeats to actin binding, we generated *Sr*Lasp variants lacking Nebulin-1, Nebulin-2, or both repeats (Figure S6A). Surface plasmon resonance (SPR) measurements showed that deletion of Nebulin-1 reduced actin-binding affinity by nearly tenfold (K_d = 2.45 μM versus 0.26 μM for wild-type *Sr*Lasp), whereas deletion of Nebulin-2 had only a modest effect (K_d = 0.37 μM) (Figures 2D, 2E, S6B and S6C). Deletion of both repeats

Langtaosha (LTS) Preprint doi: https://doi.org/10.65215/LTSpreprints.2026.11.11.000383. This version posted November 11, 2026. The copyright holder for this preprint (which was not certified by peer review) is the author/funder. Creative Commons license: CC Attribution-NonCommercial-NoDerivatives 4.0 https://creativecommons.org/licenses/by-nc-nd/4.0

abolished detectable actin binding under the conditions tested. Together, these findings identify Nebulin-1 as the principal actin-binding module of *Sr*Lasp.

*Sr*Lasp stabilizes and bundles actin filaments

To characterize the biochemical functions of *Sr*Lasp, we expressed and purified recombinant *Sr*Lasp from *Escherichia coli* (*E. coli*) (Figure S7A). Given the reported roles of Nebulin-family proteins in regulating F-actin stability[18,22], we first examined whether *Sr*Lasp affects actin dynamics using pyrene-actin assays (Figures 3A and S3B), in which pyrene fluorescence increases as pyrene-labeled actin is incorporated into filaments. *Sr*Lasp did not enhance actin polymerization under the concentrations tested (Figures S7B-S7D). We next assessed its effect on the stability of preassembled actin filaments by monitoring pyrene fluorescence decay following dilution-induced depolymerization (Figure 3A). *Arabidopsis thaliana* Villin-1 (*At*Villin-1), included as a positive control, markedly slowed the fluorescence decay, consistent with its established F-actin-stabilizing activity[23]. Similarly, *Sr*Lasp slowed the decrease in pyrene fluorescence relative to actin alone (Figure 3B). Quantification of the apparent decay rate constants (k/k_0) revealed a concentration-associated reduction in fluorescence decay at higher *Sr*Lasp concentrations, with little effect at lower concentrations (Figure 3C). These observations are consistent with a role in stabilizing actin filaments.

We next investigated whether *Sr*Lasp influences higher-order actin organization. Fluorescence imaging revealed that, whereas actin alone formed dispersed individual filaments, the addition of mCherry-tagged *Sr*Lasp induced prominent filament bundles, with *Sr*Lasp colocalizing along the bundled structures (Figures 3D and 3E). To further characterize this activity,

Langtaosha (LTS) Preprint doi: https://doi.org/10.65215/LTSpreprints.2026.11.11.000383. This version posted November 11, 2026. The copyright holder for this preprint (which was not certified by peer review) is the author/funder. Creative Commons license: CC Attribution-NonCommercial-NoDerivatives 4.0 https://creativecommons.org/licenses/by-nc-nd/4.0

we visualized actin filaments by cryo-EM across a range of *Sr*Lasp concentrations. Bundle formation was already evident at a substoichiometric *Sr*Lasp-to-actin molar ratio of approximately 0.6:1 and became increasingly prominent with higher *Sr*Lasp concentrations (Figure S7E), indicating that relatively low levels of *Sr*Lasp are sufficient to promote actin bundle formation. To quantify this activity, we performed low-speed co-sedimentation assays, in which only bundled actin filaments sediment efficiently (Figure 3F). Consistent with the imaging observations, *Sr*Lasp dramatically increased the fraction of actin recovered in the pellet compared with actin alone (Figures 3G and 3H), confirming its robust actin-bundling activity in vitro.

We next investigated whether the Nebulin repeats, which contribute to F-actin binding, are also required for actin bundling. Deletion of either repeat caused only a modest reduction in actin pelleting, and even simultaneous deletion of both repeats retained substantial bundling activity (Figures 3G and 3H). In contrast, quantification of *Sr*Lasp co-sedimentation with actin bundles revealed a stronger dependence on the Nebulin repeats. Deletion of both repeats caused the greatest reduction in *Sr*Lasp co-sedimentation, followed by deletion of Nebulin-1, whereas deletion of Nebulin-2 had a comparatively minor effect (Figure 3H). Notably, this hierarchy closely mirrored the SPR binding measurements (Figures 2D and 2E), in which Nebulin-1 contributed more strongly than Nebulin-2 to F-actin association.

Together, these findings indicate that the Nebulin repeats enhance the association of *Sr*Lasp with F-actin but are not strictly required for actin bundle formation. Thus, the contributions of the Nebulin repeats to F-actin association and bundling can be functionally distinguished, suggesting that additional regions of *Sr*Lasp support higher-order actin organization.

Langtaosha (LTS) Preprint doi: https://doi.org/10.65215/LTSpreprints.2026.11.11.000383. This version posted November 11, 2026. The copyright holder for this preprint (which was not certified by peer review) is the author/funder. Creative Commons license: CC Attribution-NonCommercial-NoDerivatives 4.0 https://creativecommons.org/licenses/by-nc-nd/4.0

Comparative structural analysis of *Sr*Lasp and vertebrate Nebulin

Having defined the actin-binding interface of *Sr*Lasp, we next investigated whether this mode of actin recognition is conserved across the Nebulin family. Although an *in situ* cryo-ET structure of mouse Nebulin bound to F-actin was previously reported at 4.5 Å resolution, the limited resolution precluded a detailed characterization of the protein–actin interface[19]. To enable a direct structural comparison, we determined a 3.0 Å cryo-EM reconstruction of the mouse Nebulin–F-actin complex from isolated skeletal-muscle thin filaments (Figures 4A, 4B and S8).

Using a consensus sequence derived from mouse Nebulin repeats for model building (Figure 2C), we found that Nebulin occupies the same actin groove as *Sr*Lasp and adopts a closely similar helix-linker-helix architecture (Figures 4C-4E). In both structures, a single Nebulin repeat extends across four consecutive actin subunits, with its N terminus oriented toward the pointed end. Structural superposition revealed extensive overlap in their actin-binding configurations, despite local structural differences, particularly in the positioning of Helix-2 (Figure 4E).

At the molecular level, helix-1 adopts a highly conserved orientation, with Asp73, Pro75, and Lys81 forming analogous contacts with actin subunits (Figure 4E). By contrast, Helix-2 exhibits greater structural divergence. Although the conserved Tyr92 and Tyr96 residues are positioned near the actin surface in both proteins, their interactions differ due to a shift in Helix-2 positioning. In *Sr*Lasp, Lys94 and Gln95 form hydrogen bonds with residues lining the actin groove, whereas Asp89, Arg90, and Lys102 in mouse Nebulin establish additional interactions with actin.

Langtaosha (LTS) Preprint doi: https://doi.org/10.65215/LTSpreprints.2026.11.11.000383. This version posted November 11, 2026. The copyright holder for this preprint (which was not certified by peer review) is the author/funder. Creative Commons license: CC Attribution-NonCommercial-NoDerivatives 4.0 https://creativecommons.org/licenses/by-nc-nd/4.0

Together, these findings reveal a conserved mode of F-actin recognition shared by *Sr*Lasp and vertebrate Nebulin, despite their evolutionary divergence. This structural conservation suggests that the fundamental actin-binding mechanism of the Nebulin family was established before the emergence of metazoans.

An ancestral mode of Nebulin-family actin organization

Although *Sr*Lasp and vertebrate Nebulin share a conserved actin-binding interface, they differ markedly in their organization along actin filaments. Vertebrate Nebulin is a giant protein containing over 100 tandem Nebulin repeats, which form a continuous array along the thin filament. By contrast, *Sr*Lasp contains merely two nebulin-like repeats flanked by an N-terminal LIM domain and two C-terminal SH3 domains, and engages F-actin through a single repeat with a 1:1 binding stoichiometry.

To compare their modes of filament association, we mapped the actin-bound Nebulin repeats of both proteins onto F-actin (Figure 5). Despite striking differences in size and repeat number, the actin-binding modules occupy equivalent positions within the actin groove and share the same orientation relative to filament polarity. In vertebrate skeletal muscle, tandem Nebulin repeats form a continuous array along F-actin. By contrast, each *Sr*Lasp molecule contributes only a single actin-bound Nebulin repeat, producing a discontinuous, paired organization along the filament.

Langtaosha (LTS) Preprint doi: https://doi.org/10.65215/LTSpreprints.2026.11.11.000383. This version posted November 11, 2026. The copyright holder for this preprint (which was not certified by peer review) is the author/funder. Creative Commons license: CC Attribution-NonCommercial-NoDerivatives 4.0 https://creativecommons.org/licenses/by-nc-nd/4.0

These findings suggest that the actin-binding mechanism characteristic of vertebrate Nebulin was already present in a unicellular relative of animals. The paired organization observed for *Sr*Lasp may represent an ancestral mode of Nebulin-family association with F-actin, whereas expansion of tandem Nebulin repeats could have enabled the continuous filament decoration characteristic of vertebrate skeletal muscle. Together, these observations provide a structural framework for understanding how an evolutionarily conserved actin-binding module may have been adapted to distinct filament architectures.

*Sr*Fascin-mediated microvillar hexagonal actin bundle

To determine the native organization of microvillar actin bundles, we performed subtomogram averaging of cryo-ET data, obtaining an initial reconstruction at ~13 Å resolution. Using this reconstruction as a reference, we further analyzed single-particle cryo-EM images of microvilli, yielding reconstructions of the central actin bundle at 4.36 Å and a larger region of the bundle at 5.79 Å resolution (Figures S9A-S9E). Further 3D classification revealed two distinct bundle architectures: a narrower bundle containing seven actin filaments resolved at 7.42 Å and a wider bundle containing an additional 12 peripheral filaments arranged in an approximately hexagonal pattern, resolved at 7.44 Å (Figures 6A and S10A–S10C). The higher-resolution reconstructions further resolved the molecular organization of the central actin bundle (Figure 6B; Movie S3).

Additional densities bridging adjacent actin filaments were observed throughout the bundle. Based on their morphology and structural compatibility with the Fascin fold, we assigned these densities to *Sr*Fascin (*S. rosetta* Fascin; UniProt: F2UQD9). An AlphaFold-predicted model of *Sr*Fascin, comprising four β-trefoil domains (β1–β4), was well fitted into the cryo-EM density map

Langtaosha (LTS) Preprint doi: https://doi.org/10.65215/LTSpreprints.2026.11.11.000383. This version posted November 11, 2026. The copyright holder for this preprint (which was not certified by peer review) is the author/funder. Creative Commons license: CC Attribution-NonCommercial-NoDerivatives 4.0 https://creativecommons.org/licenses/by-nc-nd/4.0

(Figure 6C). The fitted model revealed two distinct actin-binding interfaces: the β1/β4 surface contacts two consecutive actin subunits on one filament, whereas the β2/β3 surface engages two consecutive subunits on the neighboring filament, thereby crosslinking adjacent filaments (Figure 6C).

To examine the geometric organization of these filaments, we compared equivalent axial positions across the seven filaments using actin-bound ATP as a reference. The corresponding planes were nearly parallel and approximately perpendicular to the bundle axis, indicating that the actin filaments are aligned with remarkably similar polarity and orientation throughout the bundle. In cross-section, the six peripheral filaments were distributed at approximately 60° intervals around the central filament (Figure 7A). The axial rise between successive actin subunits was approximately 27.6 Å, corresponding to a 13-subunit helical repeat of ~358.8 Å. *Sr*Fascin crosslinks adjacent actin filaments, with a periodic arrangement repeating approximately every 13 actin subunits along the filament axis (Figure 7B).

To understand the structural arrangement of *Sr*Fascin within the bundle, we analyzed the helical geometry of F-actin (Figure 7C). F-actin typically adopts an approximately 13/6 helical arrangement, although its helical twist exhibits some variability[24,25]. To simplify the geometric analysis, we used an idealized 13/6 symmetry, corresponding to an azimuthal rotation of 166.15° between successive actin subunits (i and i+1). Under this approximation, subunits i and i+2 along the same long-pitch strand differ by ~27.7°, whereas subunits i and i+4 differ by ~55.4°. Notably, this 55.4° progression differs from the ideal 60° angular separation between neighboring filaments in the hexagonal bundle, introducing a geometric mismatch of approximately 4.6° per binding step.

Langtaosha (LTS) Preprint doi: https://doi.org/10.65215/LTSpreprints.2026.11.11.000383. This version posted November 11, 2026. The copyright holder for this preprint (which was not certified by peer review) is the author/funder. Creative Commons license: CC Attribution-NonCommercial-NoDerivatives 4.0 https://creativecommons.org/licenses/by-nc-nd/4.0

Mapping individual *Sr*Fascin molecules along the central filament revealed a strikingly ordered binding pattern (Figure 7D; Movie S4). Successive crosslinks predominantly followed an i-to-i+4 register, corresponding to a 55.4° azimuthal progression around the central actin filament. However, this regular pattern was interrupted at one position, where the next *Sr*Fascin molecule bound at an i-to-i+6 register rather than i-to-i+4. This transition introduced an additional 27.7° rotation, resulting in an angular step of 83.1°, after which the i-to-i+4 periodicity resumed (Figure 7D). We refer to this discontinuity as a Fascin “skip” event.

Closer inspection revealed that the skip was accompanied by a change in the orientation of *Sr*Fascin relative to the central actin filament. In the predominant binding orientation, designated state "a", the β1/β4 surface of *Sr*Fascin contacts the central filament, whereas the β2/β3 surface engages the neighboring filament. At the transition, this arrangement is reversed, with the β2/β3 surface contacting the central filament, defining an alternative binding orientation termed state "b" (Figures 7D and 7E). We refer to this change in binding orientation as a Fascin **“**flip” event. Previous studies have also reported changes in Fascin-binding orientation, along with conformational adjustments that allow Fascin to accommodate different interfilament geometries [26]. Conformational flexibility may allow Fascin to accommodate small geometric deviations, and switching its binding orientation could extend the range of positions at which crosslinks can form.

To explore the potential geometric significance of these transitions, we examined the spatial relationship between successive Fascin-binding sites within the hexagonal lattice. Because the predominant i-to-i+4 progression advances by approximately 55.4°, rather than the ideal 60°

Langtaosha (LTS) Preprint doi: https://doi.org/10.65215/LTSpreprints.2026.11.11.000383. This version posted November 11, 2026. The copyright holder for this preprint (which was not certified by peer review) is the author/funder. Creative Commons license: CC Attribution-NonCommercial-NoDerivatives 4.0 https://creativecommons.org/licenses/by-nc-nd/4.0

separation between neighboring filament positions, each successive binding step introduces an angular deviation of ~4.6°. If the same binding register is maintained, these deviations progressively accumulate to approximately −4.6°, −9.2°, and −13.8° relative to the ideal hexagonal geometry (Figures 7F and 7G). The observed i-to-i+6 skip introduces an additional 27.7° rotation, shifting the accumulated deviation from approximately −13.8° to +13.9°. Importantly, although the magnitude of the mismatch remains similar immediately after the skip, its direction is reversed. Subsequent i-to-i+4 binding steps can therefore progressively reduce the deviation rather than allowing it to continue accumulating (Figure 7G). Also, when the angular deviation approaches half of 27.7°, Fascin may flip to accommodate the change in binding geometry (Figure 7G).

Together, these observations reveal a highly ordered yet adaptable Fascin-crosslinked actin architecture. The predominant i-to-i+4 binding pattern establishes regular crosslinking along the actin helix, whereas occasional i-to-i+6 skipping and alternative Fascin-binding orientations provide complementary structural mechanisms that may accommodate the geometric mismatch between the helical symmetry of F-actin and the hexagonal organization of the microvillar bundle.

DISCUSSION

Our study reveals a deeply conserved actin-binding architecture shared by the ancestral Nebulin-family protein *Sr*Lasp and vertebrate Nebulin, suggesting that the molecular basis of Nebulin-family actin recognition emerged before the origin of animals. Despite their striking differences in size and domain organization, *Sr*Lasp and Nebulin occupy the same inner groove of F-actin, share a conserved binding polarity, and engage actin through similar helix–linker–helix motifs. These structural similarities suggest that the fundamental actin-binding mechanism was established

Langtaosha (LTS) Preprint doi: https://doi.org/10.65215/LTSpreprints.2026.11.11.000383. This version posted November 11, 2026. The copyright holder for this preprint (which was not certified by peer review) is the author/funder. Creative Commons license: CC Attribution-NonCommercial-NoDerivatives 4.0 https://creativecommons.org/licenses/by-nc-nd/4.0

before the extensive expansion of Nebulin repeats in vertebrates. Notably, *Sr*Lasp and Nebulin exhibit distinct modes of association with F-actin. Whereas the short Nebulin-repeat region of *Sr*Lasp adopts a paired binding mode, vertebrate Nebulin forms a continuous array along the filament. These observations suggest that a conserved molecular recognition mechanism can support different modes of filament association, potentially reflecting the diversification of Nebulin-family proteins during evolution.

One unexpected finding of this study is that several distinctive properties of *Sr*Lasp extend beyond the actin-binding functions encoded by its conserved Nebulin repeats. Full-length *Sr*Lasp eluted near the void volume in size-exclusion chromatography, much earlier than expected for its molecular weight. This early-eluting profile was largely unchanged after deletion of the LIM domain or Nebulin repeats, but shifted substantially toward later fractions upon removal of the SH3-containing region; conversely, insertion of the *S. rosetta* linker2-SH3-2 module shifted human Lasp-1 toward earlier elution (Figure S11A). Although early elution alone does not establish oligomerization, these observations suggest that the SH3-containing region contributes to the unusual solution behavior of *Sr*Lasp.

Most metazoan Lasp contain only a single SH3 domain like human, whereas many choanoflagellate Lasp homologs have two or more SH3 domains (Blast Database: Transciptome Shotgun Assembly (TSA) limited by Chonoflagellata (taxid: 28009)[27]) (Figure S11B). Lasp proteins also contain proline-rich motifs (PRMs) within their linker regions. Because SH3 domains commonly recognize PRMs through conserved xP-binding pockets[28,29], the expanded SH3 domains and PRMs of choanoflagellate Lasp proteins raise the possibility of additional

Langtaosha (LTS) Preprint doi: https://doi.org/10.65215/LTSpreprints.2026.11.11.000383. This version posted November 11, 2026. The copyright holder for this preprint (which was not certified by peer review) is the author/funder. Creative Commons license: CC Attribution-NonCommercial-NoDerivatives 4.0 https://creativecommons.org/licenses/by-nc-nd/4.0

intramolecular or intermolecular interactions. Consistent with idea functional contribution from regions outside the Nebulin repeats, deletion of the Nebulin repeats reduced F-actin association but did not abolish bundling activity (Figures 3G and 3H), whereas removal of the SH3-containing region largely eliminated bundle formation (Figures S11C and S11E). In parallel assays with human Lasp, *Hs*Lasp-1 showed little bundling activity, whereas *Hs*Lasp-2 promoted F-actin bundling (Figures S11D and S11F), consistent with previous reports that Lasp-2 associates with filopodial actin bundles and binds F-actin[30]. Moreover, transplantation of the *S. rosetta* linker2-SH3-2 region conferred robust bundling activity upon *Hs*Lasp-1 (Figures S11D and S11F). Furthermore, deletion of SH3 did not abolish F-actin association but altered its binding kinetics from a slow-association, slow-dissociation mode to a substantially faster binding regime (Figure S11G).

Together, these observations suggest that the SH3 domain influences not only the solution behavior of *Sr*Lasp but also how it interacts with and organizes actin filaments. Although the molecular basis of these effects remains unresolved, SH3-mediated interactions may contribute to the prolonged association of *Sr*Lasp with F-actin and facilitate filament crosslinking. Unlike vertebrate Nebulin, which contains an extensive array of actin-binding repeats, *Sr*Lasp combines a short Nebulin-repeat region with additional domains that contribute to its actin-associated functions. This distinction raises the possibility that Nebulin-family proteins have evolved different strategies for organizing and regulating actin filaments, combining a conserved actin-binding interface with diversification of their surrounding domain architectures.

Langtaosha (LTS) Preprint doi: https://doi.org/10.65215/LTSpreprints.2026.11.11.000383. This version posted November 11, 2026. The copyright holder for this preprint (which was not certified by peer review) is the author/funder. Creative Commons license: CC Attribution-NonCommercial-NoDerivatives 4.0 https://creativecommons.org/licenses/by-nc-nd/4.0

A second notable finding is the prominent role of Fascin in organizing the *S. rosetta* microvillar actin bundle. In vertebrates, microvillar actin bundles are predominantly organized by Villin-, Espin-, and Plastin-family proteins[31], whereas Fascin is more commonly associated with filopodia and other dynamic actin-based protrusions[32]. Notably, previous immunolocalization studies have identified Fascin within the actin-filled collar of *S. rosetta*[12], and our *in situ* reconstruction now provides direct structural evidence for its extensive involvement in microvillar actin crosslinking This difference in crosslinker usage raises the possibility that the organization of parallel actin bundles is more evolutionarily conserved than the specific proteins responsible for their assembly. Rather than relying on a fixed set of crosslinkers, microvilli may employ different combinations of actin-binding proteins across species to achieve similar cytoskeletal architectures.

The evolutionary conservation revealed here may also have implications for understanding human Lasp proteins. Lasp-1 was first identified in metastatic lymph nodes from breast cancer patients[33]. It has been implicated in cell migration, invasion, and metastasis[34], and its elevated expression is associated with poor clinical outcomes in several cancers (Figures S12A and S12B). Nevertheless, the structural basis of human Lasp-1 association with F-actin remains unresolved. The strong conservation of the Nebulin-family actin-binding motif across filozoans suggests that key features of the interface may have been maintained during evolution (Figure S12C). Although the actin-bound structure of human Lasp-1 remains unresolved, the conserved binding architecture revealed here provides a structural framework for understanding Lasp-actin interactions and their potential relevance to human disease.

Langtaosha (LTS) Preprint doi: https://doi.org/10.65215/LTSpreprints.2026.11.11.000383. This version posted November 11, 2026. The copyright holder for this preprint (which was not certified by peer review) is the author/funder. Creative Commons license: CC Attribution-NonCommercial-NoDerivatives 4.0 https://creativecommons.org/licenses/by-nc-nd/4.0

In summary, our findings reveal that key principles of microvillar actin organization emerged before the origin of animals. The actin-binding mechanism of the Nebulin family was already established in choanoflagellates and subsequently retained throughout filozoan evolution, while Fascin-based bundle organization suggests that fundamental features of the microvillar cytoskeleton predate the diversification of animal-specific actin regulators. Together, these results provide a molecular framework for understanding the evolutionary origins of actin-based cellular protrusions and illuminate an ancestral mode of microvillar organization that existed before the emergence of multicellular animals.

Limitations of the study

Our structural and biochemical analyses reveal how *Sr*Lasp interacts with F-actin and promotes actin bundling in vitro. However, its physiological role in microvilli remains to be validated through genetic studies in *S. rosetta*. In addition, the native architecture of microvillar actin bundles has not been reconstituted in vitro. Their assembly may depend on additional cellular factors and regulatory mechanisms. Further studies are needed to understand how this architecture is established and maintained *in vivo*. Finally, our structural comparison of *Sr*Lasp and vertebrate Nebulin is limited to two species. Broader phylogenetic sampling and structural characterization will be necessary to clarify the evolution of distinct actin-binding modes within the Nebulin family.

Langtaosha (LTS) Preprint doi: https://doi.org/10.65215/LTSpreprints.2026.11.11.000383. This version posted November 11, 2026. The copyright holder for this preprint (which was not certified by peer review) is the author/funder. Creative Commons license: CC Attribution-NonCommercial-NoDerivatives 4.0 https://creativecommons.org/licenses/by-nc-nd/4.0

Figures and legends

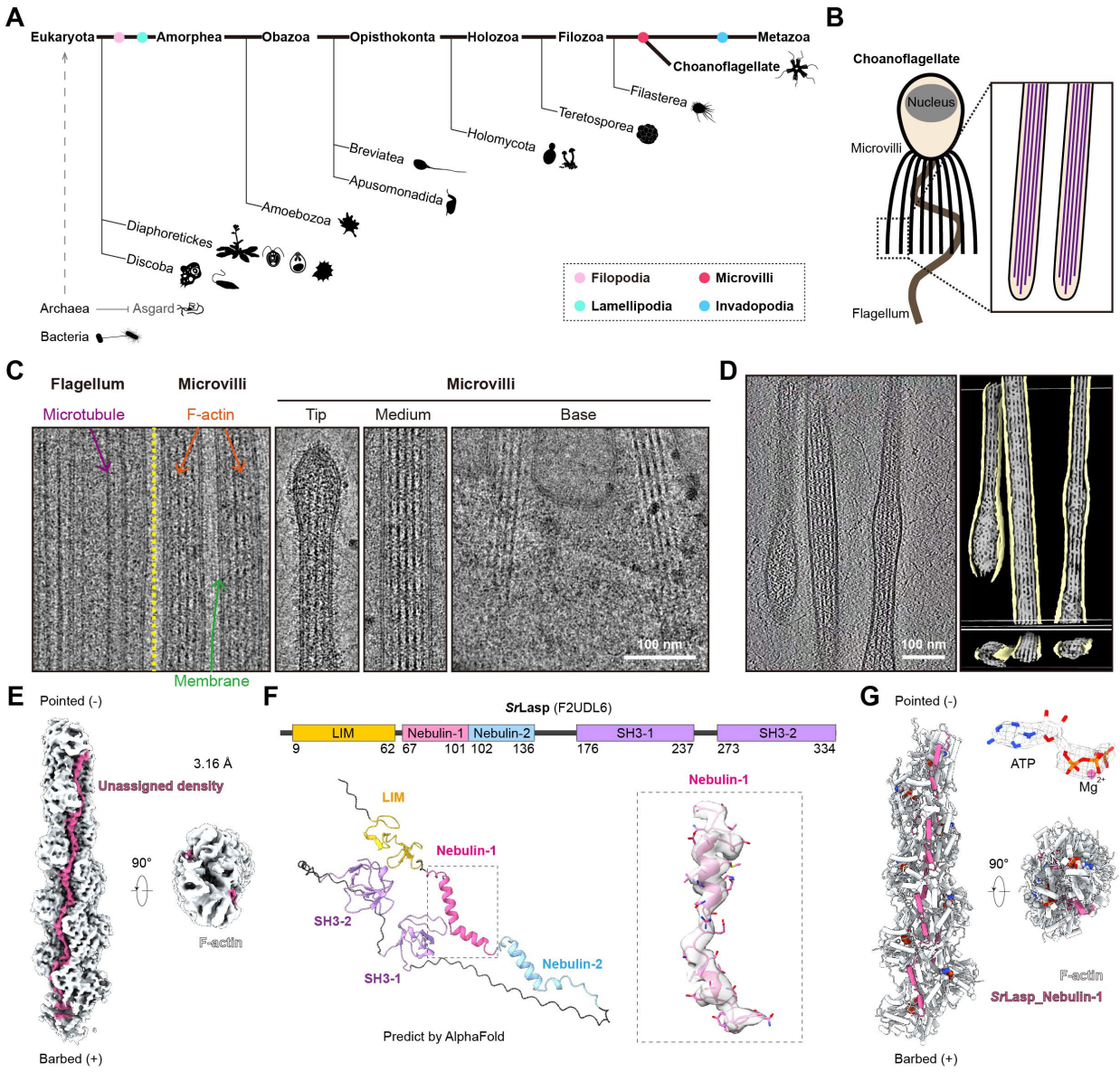


Figure 1. A Nebulin-family protein associated with microvillar actin filaments in *S. rosetta*

(A) Distribution of major actin-based protrusion types across eukaryotic evolution. Simplified phylogeny showing the inferred evolutionary emergence of lamellipodia, filopodia, microvilli, and invadopodia. Choanoflagellates occupy a key phylogenetic position as the closest unicellular relatives of animals and possess prominent microvillar collars. Organism silhouettes were obtained

Langtaosha (LTS) Preprint doi: https://doi.org/10.65215/LTSpreprints.2026.11.11.000383. This version posted November 11, 2026. The copyright holder for this preprint (which was not certified by peer review) is the author/funder. Creative Commons license: CC Attribution-NonCommercial-NoDerivatives 4.0 https://creativecommons.org/licenses/by-nc-nd/4.0

from PhyloPic (https://www.phylopic.org/). **(B)** Schematic representation of the choanoflagellate *S. rosetta*. The cell is surrounded by a collar of actin-rich microvilli and bears a single apical flagellum. The boxed region illustrates the parallel actin filament bundles that form the microvillar core. **(C)** Representative cryo-EM micrographs of *S. rosetta* flagella and microvilli. Longitudinal views of microvilli from the tip, middle, and basal regions reveal highly ordered filamentous densities throughout the protrusion. Scale bar, 100 nm. **(D)** Representative microvillus selected for cryo-ET analysis. Left, raw cryo-ET image. Right, corresponding volume segmentation and cross-sectional views. Scale bar, 100 nm. **(E)** Cryo-EM reconstruction of the microvillar actin filament at 3.16 Å resolution. An additional density (magenta) is observed within the major groove of F-actin and extends continuously along the filament. Orthogonal view is shown. **(F)** Identification of a candidate Nebulin-family protein in *S. rosetta*. Top, domain architecture of the putative Lasp homolog F2UDL6, containing one LIM domain, two Nebulin repeats, and two SH3 domains. Bottom left, AlphaFold-predicted full-length structure. Bottom right, cryo-EM density fitted with the refined Nebulin-1 model derived from the first nebulin repeat. **(G)** Atomic model of the actin-bound *Sr*Lasp Nebulin-1 repeat. The Nebulin-1 repeat (magenta) occupies the major groove of F-actin and extends across multiple actin subunits with a defined polarity from the pointed end toward the barbed end. Insets show ATP and Mg^{2+} densities.

Langtaosha (LTS) Preprint doi: https://doi.org/10.65215/LTSpreprints.2026.11.11.000383. This version posted November 11, 2026. The copyright holder for this preprint (which was not certified by peer review) is the author/funder. Creative Commons license: CC Attribution-NonCommercial-NoDerivatives 4.0 https://creativecommons.org/licenses/by-nc-nd/4.0

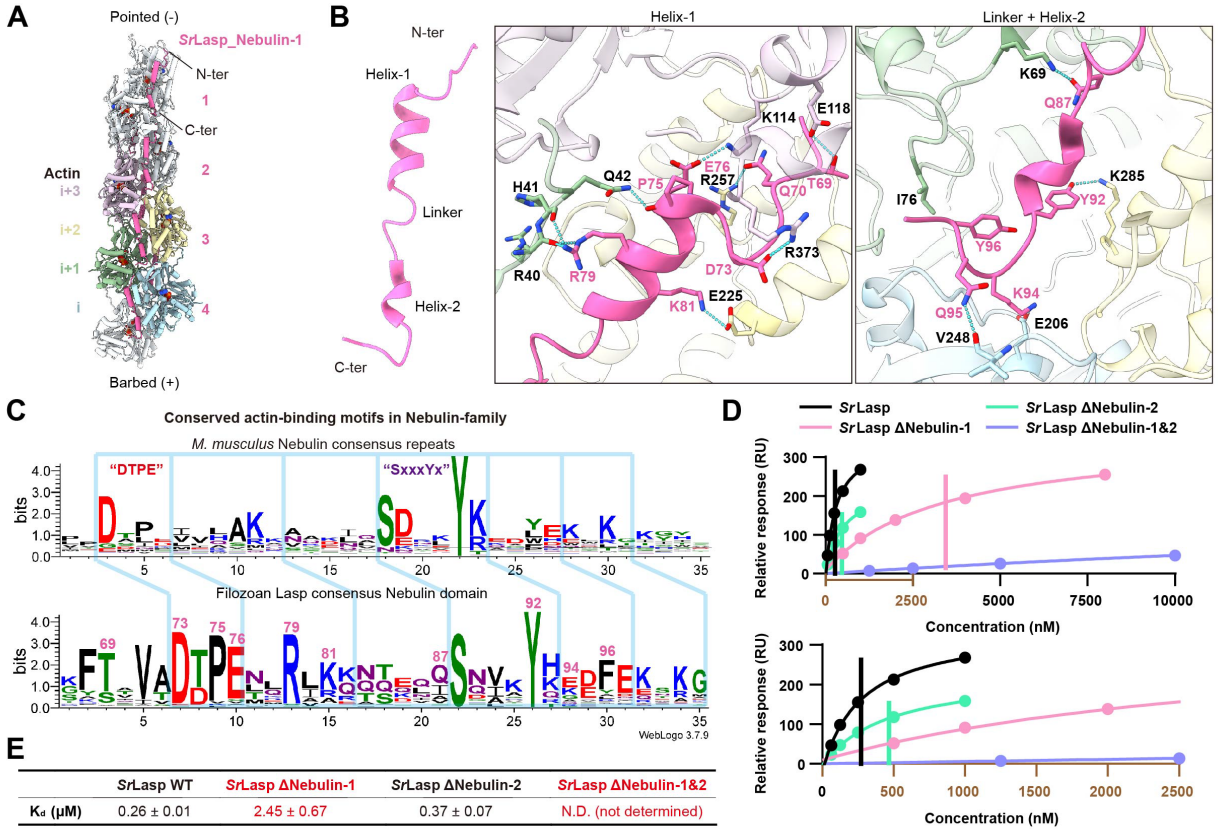


Figure 2. Structural basis of F-actin recognition by *Sr*Lasp

(A) Atomic model of the *Sr*Lasp Nebulin-1 repeat bound to F-actin. The *Sr*Lasp Nebulin-1 repeat (magenta) spans four consecutive actin subunits (labeled i to i+4). The repeat is oriented with its N-terminus toward the pointed end and its C-terminus toward the barbed end. Actin protomers are shown in different colors to illustrate the binding register. **(B)** Molecular interactions between *Sr*Lasp Nebulin-1 and F-actin. Left, interactions formed by Helix-1. Right, interactions mediated by the linker and Helix-2. Residues participating in the interface are shown as sticks. Hydrogen bonds are indicated by cyan dashed lines. Single-letter abbreviations for the amino acid residues are as follows: T, Thr; E, Glu; Q, Gln; R, Arg; D, Asp; P, Pro; K, Lys; H, His; I, Ile; V, Val; and Y, Tyr. **(C)** Sequence conservation of Nebulin repeats. Sequence logos derived from mouse Nebulin repeats (top) and filozoan Lasp Nebulin repeats (bottom) reveal conservation of

Langtaosha (LTS) Preprint doi: https://doi.org/10.65215/LTSpreprints.2026.11.11.000383. This version posted November 11, 2026. The copyright holder for this preprint (which was not certified by peer review) is the author/funder. Creative Commons license: CC Attribution-NonCommercial-NoDerivatives 4.0 https://creativecommons.org/licenses/by-nc-nd/4.0

characteristic actin-binding motifs, including the SxxxYx motif and the DTPE-containing region. Conserved residues implicated in actin binding are highlighted by their relative enrichment across the family. Interaction residues of *Sr*Lasp number is shown. **(D)** Steady-state binding analysis of *Sr*Lasp and Nebulin-repeat deletion variants measured by surface plasmon resonance (SPR) using immobilized F-actin. Top, equilibrium binding responses over the full concentration range for wild-type *Sr*Lasp, *Sr*LaspΔNebulin-1, *Sr*LaspΔNebulin-2, and *Sr*LaspΔNebulin-1&2. Bottom, enlarged view of the 0–2500 nM concentration range shown in the top panel. Curves represent steady-state fits of equilibrium binding responses. **(E)** Binding affinities (K_d) derived from steady-state fitting of the equilibrium binding responses. Values are presented as mean ± SEM from three independent experiments. N.D., not determined.

Langtaosha (LTS) Preprint doi: https://doi.org/10.65215/LTSpreprints.2026.11.11.000383. This version posted November 11, 2026. The copyright holder for this preprint (which was not certified by peer review) is the author/funder. Creative Commons license: CC Attribution-NonCommercial-NoDerivatives 4.0 https://creativecommons.org/licenses/by-nc-nd/4.0

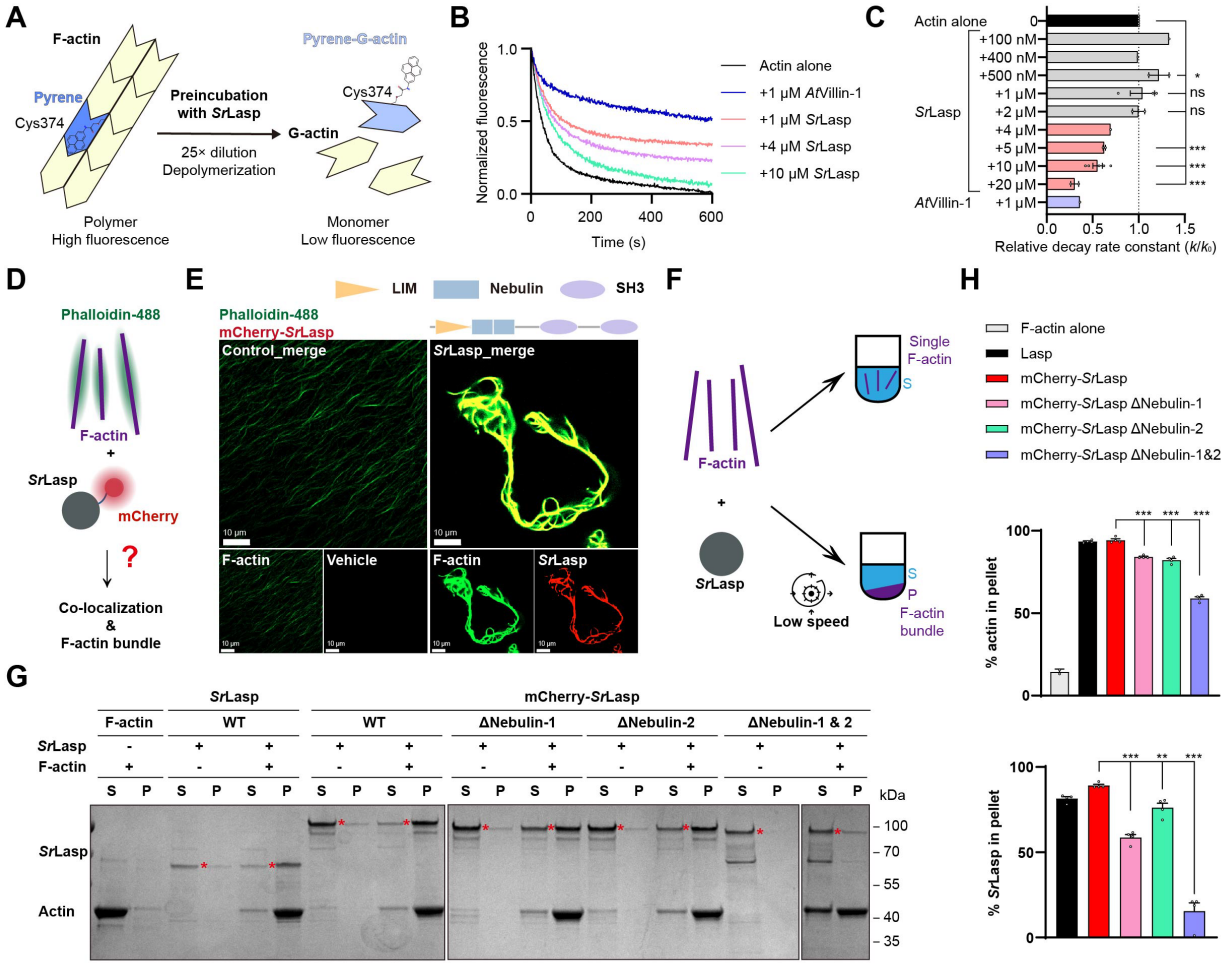


Figure 3. *Sr*Lasp stabilizes and bundles actin filaments

(A) Schematic of the pyrene-actin depolymerization assay. Preassembled pyrene-labeled F-actin was incubated with *Sr*Lasp before depolymerization was initiated by 25-fold dilution. Depolymerization was monitored by the decrease in pyrene fluorescence. **(B)** Representative normalized pyrene-actin depolymerization traces in the absence or presence of the indicated concentrations of *Sr*Lasp or *At*Villin-1. Fluorescence traces were aligned to a common initial intensity and normalized using the corresponding actin-alone control. **(C)** Relative apparent fluorescence decay rate constants (k/k_0), normalized to the corresponding actin-alone control within each independent experiment. Data are presented as mean ± SEM where applicable (n = 1–

Langtaosha (LTS) Preprint doi: https://doi.org/10.65215/LTSpreprints.2026.11.11.000383. This version posted November 11, 2026. The copyright holder for this preprint (which was not certified by peer review) is the author/funder. Creative Commons license: CC Attribution-NonCommercial-NoDerivatives 4.0 https://creativecommons.org/licenses/by-nc-nd/4.0

4 independent experiments per condition). Technical replicates were averaged within each experiment. Data are presented as mean ± SEM. Statistical significance was assessed using a two-tailed unpaired Student's t-test. ns, not significant, *P < 0.05, **P < 0.01, ***P < 0.001. **(D)** Experimental design for visualization of *Sr*Lasp-induced actin bundling. Alexa Fluor 488–phalloidin–labeled F-actin was incubated with mCherry-tagged *Sr*Lasp and examined by fluorescence microscopy to assess colocalization and bundle formation. **(E)** Fluorescence microscopy analysis of actin filament organization. Left, control actin filaments in the absence of *Sr*Lasp. Right, after incubation of *Sr*Lasp and F-actin at high molar ratios >10:1. Green, F-actin; red, mCherry-*Sr*Lasp. Scale bars, 10 μm. Representative images from three independent experiments are shown. **(F)** Schematic representation of the low-speed co-sedimentation assay used to quantify actin bundle formation. Individual actin filaments remain in the supernatant (S), whereas bundled filaments sediment into the pellet (P) under low-speed centrifugation. **(G)** Representative SDS–PAGE analysis of low-speed co-sedimentation assays performed with wild-type *Sr*Lasp and Nebulin-repeat deletion variants. Supernatant (S) and pellet (P) fractions were analyzed to assess actin bundling activity. Representative images from three independent experiments are shown. **(H)** Quantification of low-speed co-sedimentation assays. Top, percentage of total actin recovered in the pellet fraction. Bottom, percentage of total *Sr*Lasp recovered in the pellet fraction. Data are presented as mean ± SEM. Statistical significance was assessed using a two-tailed unpaired Student's t-test. *P < 0.05, **P < 0.01, ***P < 0.001.

Langtaosha (LTS) Preprint doi: https://doi.org/10.65215/LTSpreprints.2026.11.11.000383. This version posted November 11, 2026. The copyright holder for this preprint (which was not certified by peer review) is the author/funder. Creative Commons license: CC Attribution-NonCommercial-NoDerivatives 4.0 https://creativecommons.org/licenses/by-nc-nd/4.0

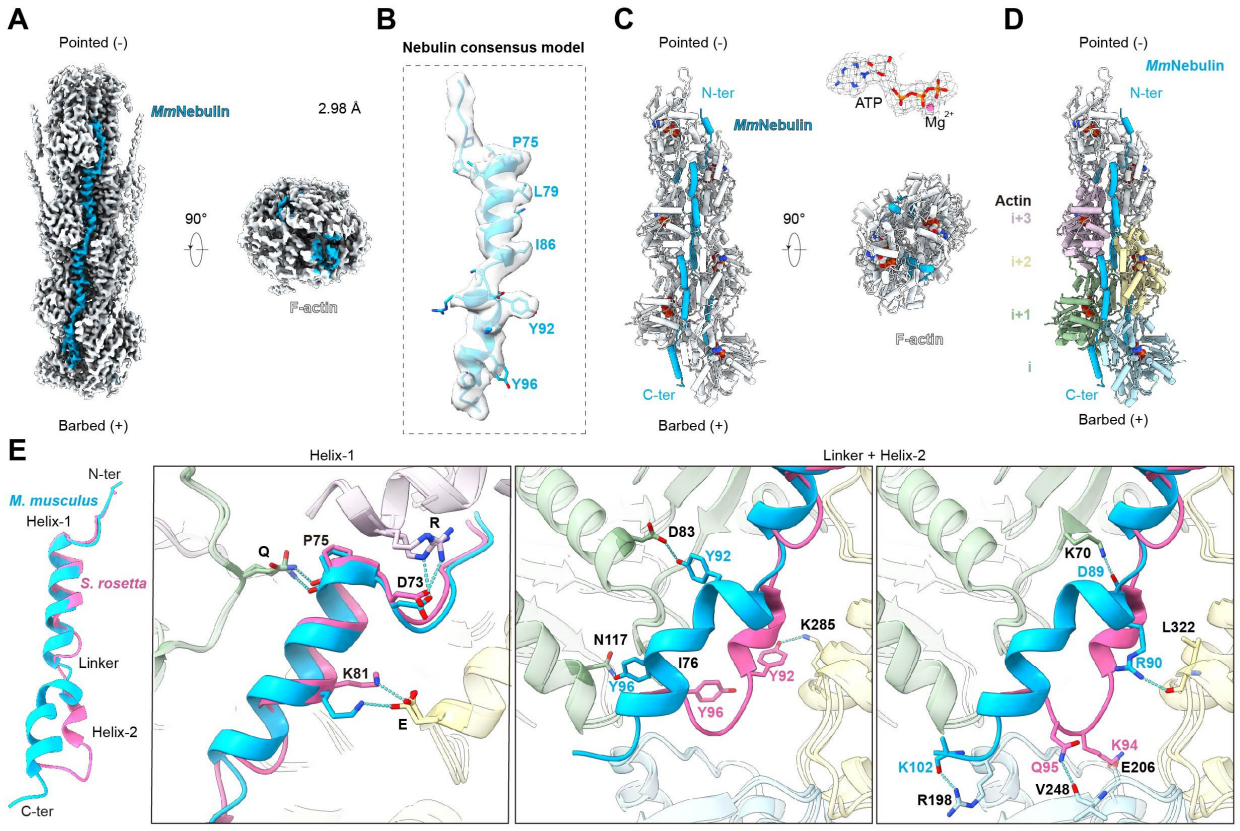


Figure 4. Conserved actin-binding architecture of *Sr*Lasp and vertebrate Nebulin

(A) Cryo-EM reconstruction of the mouse skeletal muscle thin filament at 2.98 Å resolution. Continuous density corresponding to Nebulin (cyan) is observed within the major groove of F-actin. Orthogonal views are shown. **(B)** Cryo-EM density fitted with the refined mouse Nebulin model of consensus repeat sequence. The density is well resolved and supports unambiguous model building of the actin-bound Nebulin repeat. **(C)** Atomic model of the mouse Nebulin repeat bound to F-actin. Nebulin (cyan) extends along the major groove of the filament and adopts a defined polarity with its N-terminus oriented toward the pointed end and its C-terminus toward the barbed end. Insets show ATP and Mg^{2+} densities. **(D)** Position of the mouse Nebulin repeat relative to four consecutive actin subunits (labeled i to i+4). Nebulin occupies the major groove of F-actin and spans multiple neighboring protomers. **(E)** Structural comparison of the actin-bound Nebulin

Langtaosha (LTS) Preprint doi: https://doi.org/10.65215/LTSpreprints.2026.11.11.000383. This version posted November 11, 2026. The copyright holder for this preprint (which was not certified by peer review) is the author/funder. Creative Commons license: CC Attribution-NonCommercial-NoDerivatives 4.0 https://creativecommons.org/licenses/by-nc-nd/4.0

repeat from mouse Nebulin (cyan) and *Sr*Lasp Nebulin-1 (magenta). Left, superposition of the overall fold reveals a similar helix–linker–helix architecture. Middle, conserved interface residues of Helix-1 adopt nearly identical conformations and establish equivalent polar interactions with F-actin. Right, residues in Helix-2 form different contacts with the actin filament. Hydrogen bonds are indicated by cyan dashed lines.

Langtaosha (LTS) Preprint doi: https://doi.org/10.65215/LTSpreprints.2026.11.11.000383. This version posted November 11, 2026. The copyright holder for this preprint (which was not certified by peer review) is the author/funder. Creative Commons license: CC Attribution-NonCommercial-NoDerivatives 4.0 https://creativecommons.org/licenses/by-nc-nd/4.0

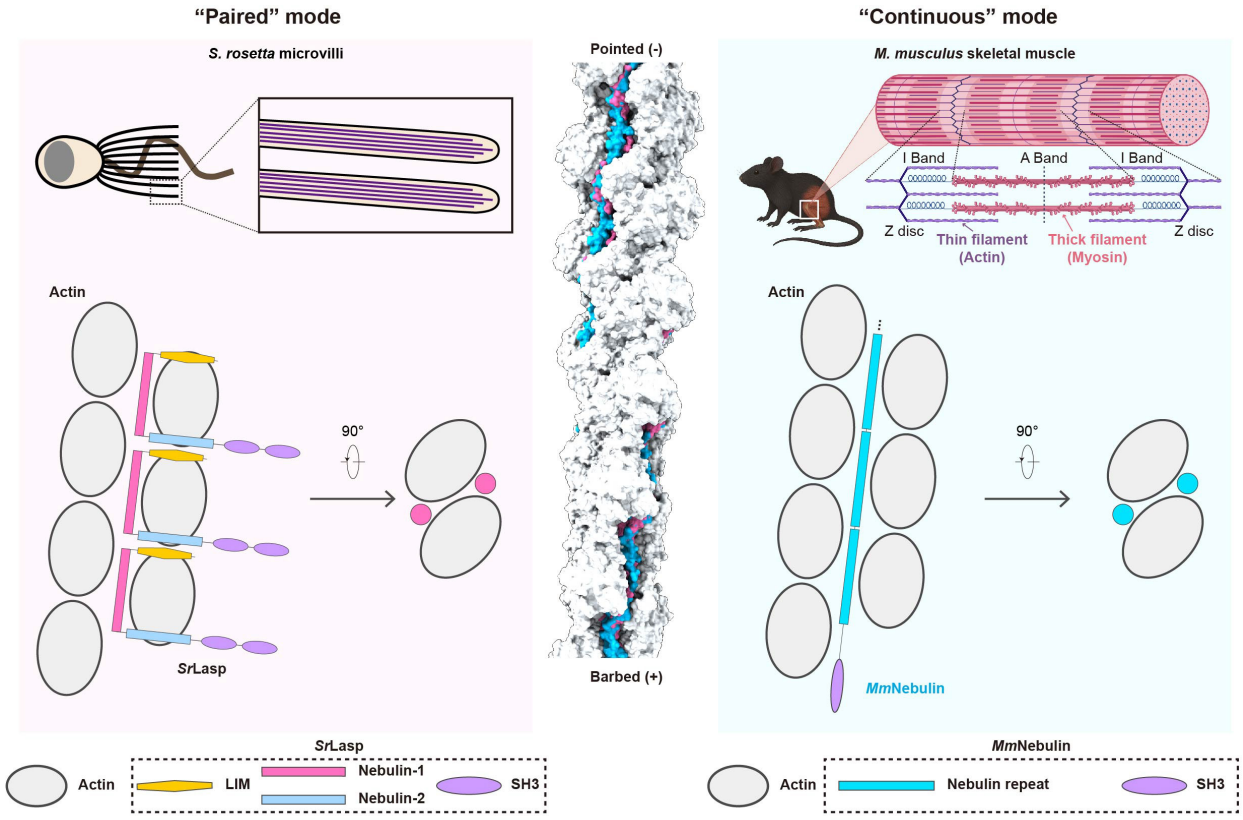


Figure 5. An ancestral mode of Nebulin-family actin organization

Comparison of Nebulin-family actin organization in *S. rosetta* microvilli and vertebrate mouse skeletal muscle. In vertebrate skeletal muscle, Nebulin contains hundreds of tandem repeats that continuously decorate thin filaments, generating a "continuous" mode of actin association along nearly the entire filament length. In contrast, *Sr*Lasp contains only two Nebulin repeats together with LIM and SH3 domains and associates with microvillar actin filaments through a "paired" mode. Despite these differences in overall architecture, mouse Nebulin (cyan) and *Sr*Lasp Nebulin-1 (magenta) occupy equivalent positions within the two major groove of F-actin and share the same polarity, with their N-termini oriented toward the pointed end and their C-termini toward the barbed end. The mouse skeletal muscle schematic was created with BioRender.com.

Langtaosha (LTS) Preprint doi: https://doi.org/10.65215/LTSpreprints.2026.11.11.000383. This version posted November 11, 2026. The copyright holder for this preprint (which was not certified by peer review) is the author/funder. Creative Commons license: CC Attribution-NonCommercial-NoDerivatives 4.0 https://creativecommons.org/licenses/by-nc-nd/4.0

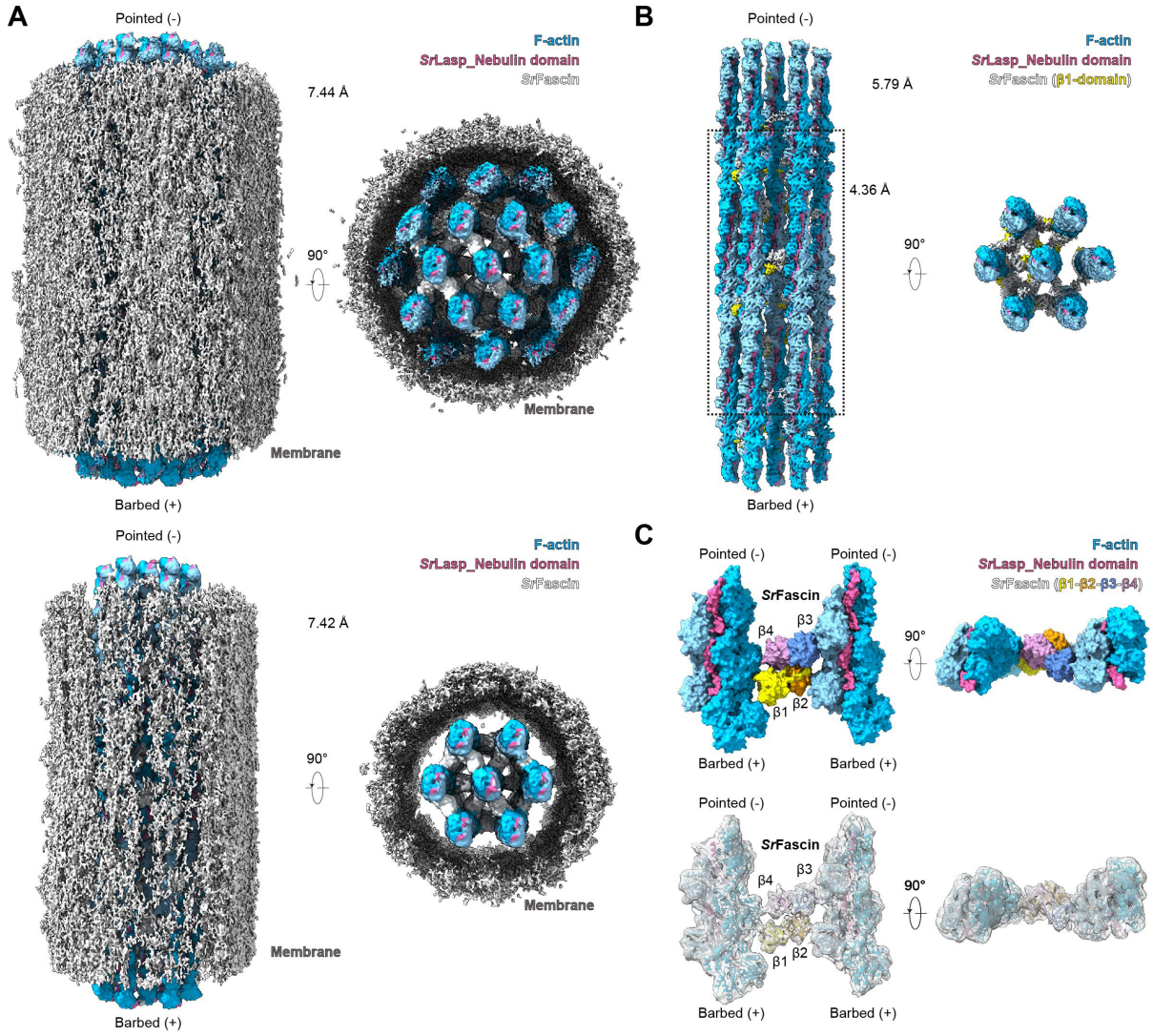


Figure 6. *In situ* structural organization of the microvillar actin bundle

(A) Cryo-EM density maps of two distinct microvillar architectures reconstructed through combined cryo-EM and cryo-ET analyses, at resolutions of 7.44 Å (top) and 7.42 Å (bottom). The wider microvillus contains a central actin core surrounded by additional filaments arranged in a hexagonal pattern, whereas the narrower microvillus is largely restricted to the central core. Longitudinal and cross-sectional views are shown, with the surrounding membrane density displayed in gray. **(B)** Cryo-EM density maps of the microvillar actin bundle at an overall resolution of 5.79 Å, with focused refinement of the central core reaching 4.36 Å (dashed box).

Langtaosha (LTS) Preprint doi: https://doi.org/10.65215/LTSpreprints.2026.11.11.000383. This version posted November 11, 2026. The copyright holder for this preprint (which was not certified by peer review) is the author/funder. Creative Commons license: CC Attribution-NonCommercial-NoDerivatives 4.0 https://creativecommons.org/licenses/by-nc-nd/4.0

Longitudinal and cross-sectional views show F-actin (sky blue), the *Sr*Lasp Nebulin domain (hot pink), and *Sr*Fascin (white, with its β1 domain highlighted in yellow). **(C)** Structural organization of the *Sr*Fascin crosslink between adjacent F-actin filaments. The upper panels show surface representations of the fitted atomic models of *Sr*Fascin, F-actin, and the *Sr*Lasp Nebulin domain in longitudinal and cross-sectional views. The lower panels show the corresponding atomic models in cartoon representation fitted into the cryo-EM density map. The AlphaFold-predicted structure of *Sr*Fascin (UniProt: F2UQD9) comprises four β-trefoil domains (β1–β4).

Langtaosha (LTS) Preprint doi: https://doi.org/10.65215/LTSpreprints.2026.11.11.000383. This version posted November 11, 2026. The copyright holder for this preprint (which was not certified by peer review) is the author/funder. Creative Commons license: CC Attribution-NonCommercial-NoDerivatives 4.0 https://creativecommons.org/licenses/by-nc-nd/4.0

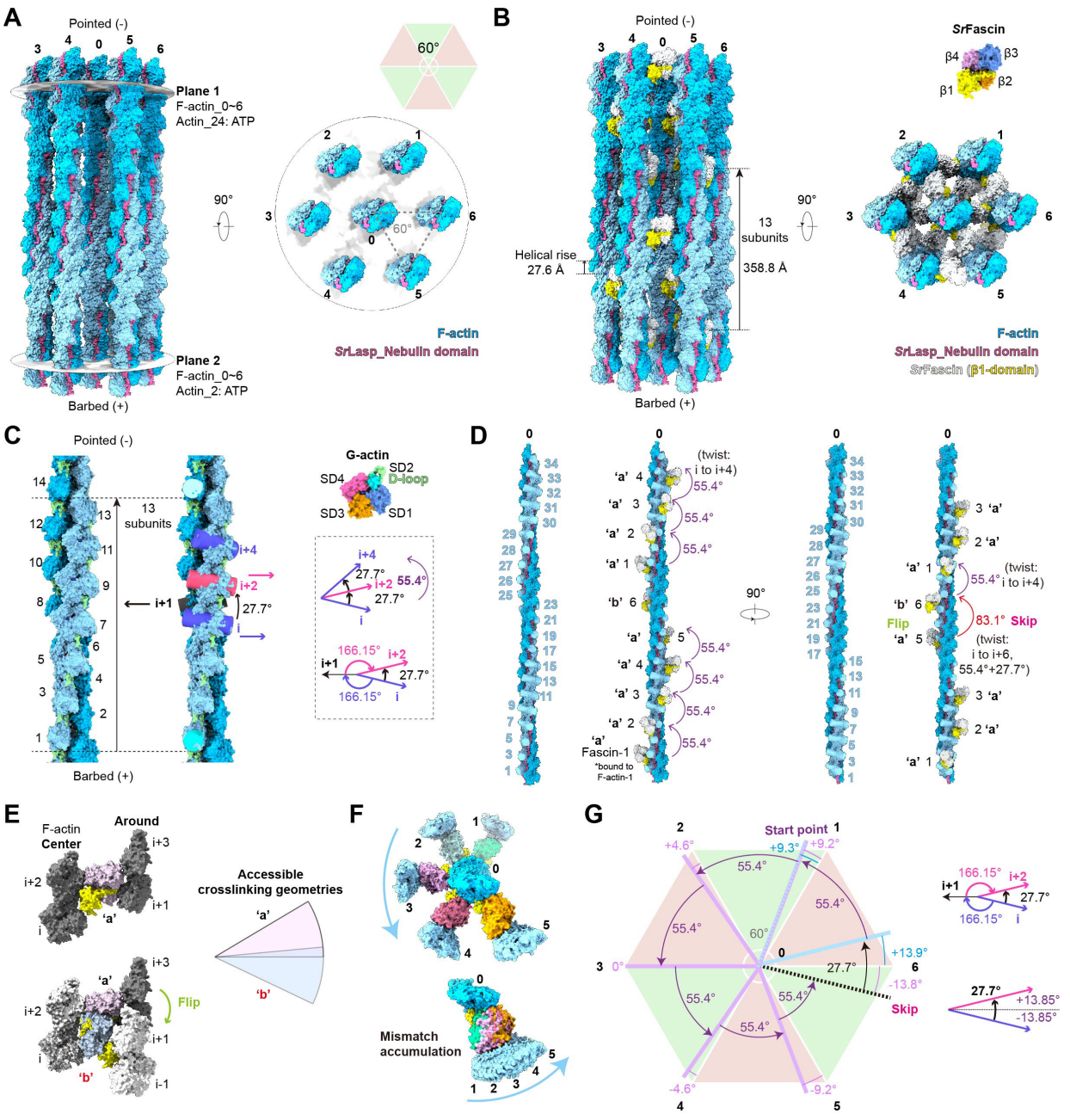


Figure 7. Structural organization and geometric adaptation of *Sr*Fascin within the microvillar actin bundle

All molecular structures are shown as surface representations of atomic models unless otherwise indicated. **(A)** Organization of the *S. rosetta* microvillar actin bundle. Seven actin filaments form a hexagonal arrangement, with one central filament (0) surrounded by six peripheral filaments (1–

Langtaosha (LTS) Preprint doi: https://doi.org/10.65215/LTSpreprints.2026.11.11.000383. This version posted November 11, 2026. The copyright holder for this preprint (which was not certified by peer review) is the author/funder. Creative Commons license: CC Attribution-NonCommercial-NoDerivatives 4.0 https://creativecommons.org/licenses/by-nc-nd/4.0

6). Comparison of equivalent axial positions, marked by actin-bound ATP molecules (planes 1 and 2), reveals a highly ordered arrangement in which the filaments share similar polarity and axial alignment. The six peripheral filaments are distributed at approximately 60° intervals around the central filament. **(B)** Distribution of *Sr*Fascin crosslinks within the microvillar actin bundle in longitudinal and cross-sectional views. The helical rise between successive actin subunits was approximately 27.6 Å, corresponding to a 13-subunit axial repeat of approximately 358.8 Å. *Sr*Fascin crosslinks adjacent actin filaments in a periodic arrangement repeating approximately every 13 actin subunits along the filament axis. **(C)** Helical geometry of F-actin. The D-loop in actin subdomain 2 (SD2) serves as a marker of filament orientation. For the geometric analysis, an idealized 13/6 helical symmetry was used, corresponding to an azimuthal rotation of 166.15° between successive actin subunits (i and i+1). Under this approximation, subunits i and i+2 differ by approximately 27.7° in azimuthal orientation, whereas subunits i and i+4 differ by approximately 55.4°. The angular relationships are illustrated schematically on the right. **(D)** Periodic distribution of *Sr*Fascin crosslinks along adjacent actin filaments. Successive *Sr*Fascin molecules predominantly bind at intervals of four actin subunits (i to i+4), corresponding to an angular progression of approximately 55.4°. At one position, this pattern is interrupted by a six-subunit interval (i to i+6), termed a "skip" event, after which the i-to-i+4 periodicity resumes. This transition is accompanied by a change in *Sr*Fascin-binding orientation from state "a" to state "b", termed a "flip" event. **(E)** Two distinct *Sr*Fascin-binding orientations, designated "a" and "b", between adjacent actin filaments. The accompanying schematic illustrates how switching between these orientations (flip) may expand the range of accessible crosslinking geometries. **(F)** Superposition of the actin subunits bound by different *Sr*Fascin molecules onto a common reference position reveals a progressive shift in the relative positions of successive *Sr*Fascin crosslinks. **(G)** Geometric model illustrating how *Sr*Fascin skip and flip events may accommodate

Langtaosha (LTS) Preprint doi: https://doi.org/10.65215/LTSpreprints.2026.11.11.000383. This version posted November 11, 2026. The copyright holder for this preprint (which was not certified by peer review) is the author/funder. Creative Commons license: CC Attribution-NonCommercial-NoDerivatives 4.0 https://creativecommons.org/licenses/by-nc-nd/4.0

angular mismatch within the hexagonal actin bundle. Successive i-to-i+4 binding events produce an angular deviation of approximately 4.6° per step relative to the ideal 60° hexagonal arrangement. An i-to-i+6 skip introduces an additional 27.7° rotation, shifting the accumulated deviation from approximately −13.8° to +13.9° and preventing further accumulation in the same direction. The accompanying flip between binding orientations "a" and "b" may enable *Sr*Fascin to accommodate this angular shift while maintaining crosslinks between adjacent filaments. The corresponding orientations are indicated by the colors used in Figure 7F.

Langtaosha (LTS) Preprint doi: https://doi.org/10.65215/LTSpreprints.2026.11.11.000383. This version posted November 11, 2026. The copyright holder for this preprint (which was not certified by peer review) is the author/funder. Creative Commons license: CC Attribution-NonCommercial-NoDerivatives 4.0 https://creativecommons.org/licenses/by-nc-nd/4.0

RESOURCE AVAILABILITY

Lead contact

Further information and requests for reagents may be directed and will be fulfilled by Chuangye Yan (yancy2019@tsinghua.edu.cn), the lead contact.

Materials availability

Data and code availability

The cryo-EM map of native mastigoneme and the corresponding atomic coordinate have been deposited in the Electron Microscopy Data Bank (https://www.ebi.ac.uk/pdbe/emdb/) and the Protein Data Bank (http://www.rcsb.org), under the accession codes EMD-85122 and 48EO, EMD-85124 and 48EQ respectively. These accession numbers are also listed in the key resources table.

EXPERIMENTAL MODEL AND STUDY PARTICIPANT DETAILS

Strains and cell culture

S. rosetta (ATCC 50818) co-cultured with *Echinicola pacifica* was a gift from Prof. Nicole King's lab. The *S. rosetta* was cultured as previously described with minor modifications (King lab choanoflagellate handbook: https://kinglab.berkeley.edu/resources/)[35]. Briefly, cells were cultured at 22 °C under 60% humidity in 5% Seawater Complete Media (SWC) diluted with artificial seawater (ASW), both made using Tropic Marin Pro-Reef Meersalz/Sea salt (Alkalinity 7-8°dH, Calcium 420-460 mg/L, Magnesium 1300-1400 mg/L). Cells were passed 1:50 every 2 days.

Langtaosha (LTS) Preprint doi: https://doi.org/10.65215/LTSpreprints.2026.11.11.000383. This version posted November 11, 2026. The copyright holder for this preprint (which was not certified by peer review) is the author/funder. Creative Commons license: CC Attribution-NonCommercial-NoDerivatives 4.0 https://creativecommons.org/licenses/by-nc-nd/4.0

METHOD DETAILS

Choanoflagellate culture and cryo-EM sample preparation

Before freezing, *S. rosetta* cultures were scaled up to 120-160 mL, pelleted at 2000 x g (4 °C, 10-15 min), resuspended in ASW, and starved for 20-24 hr to reduce excess *E. pacifica*. Starved *S. rosetta* cells were then pelleted and resuspended in a small volume of ASW (50-100 µL) shortly before plunge-freezing. Grids (Quantifoil Au R1.2/1.3, 300 mesh or 200 mesh) were glow discharged for 30-35 s using the medium power setting of the Plasma Cleaner PDC32G (Harrick). 4 µL aliquots of the sample were applied to grids. After a 60 s incubation at room temperature (RT), the grids were blotted from the opposite side of the carbon layer for 13 s before being flash-frozen in liquid ethane cooled by liquid nitrogen with Leica EM GP2 plunge freezer (Leica Microsystems, Vienna, Austria) at 22 °C and 60% humidity.

Protein expression and purification

S. rosetta Lasp (UniProt ID: F2UDL6) cDNA or domain deletion mutants were cloned into a pET15b vector with an N-terminal FLAG tag. Human Lasp-1 (UniProt ID: Q14847) and Lasp-2 (UniProt ID: Q59FZ8) cDNA or human-choanoflagellate Lasp hybrid protein were cloned into a pCAG vector with an N-terminal FLAG tag. For pET15b, plasmids were transformed into *E. coli* BL21(DE3). Cultures were induced with 0.5 mM IPTG at $OD_{600} \approx 1.0$ and incubated at 22 °C for 18 h. For pCAG, 2 mg plasmid and 4 mg polyethylenimine (YEASON) were preincubated in 50 ml fresh SMM 293-TII medium (Sino Biological) for 30 min before adding into one liter HEK293F cells at density of 2.0×10^6 cells per ml, and then incubate at 37 °C for 48 h under 5% CO_2.

Langtaosha (LTS) Preprint doi: https://doi.org/10.65215/LTSpreprints.2026.11.11.000383. This version posted November 11, 2026. The copyright holder for this preprint (which was not certified by peer review) is the author/funder. Creative Commons license: CC Attribution-NonCommercial-NoDerivatives 4.0 https://creativecommons.org/licenses/by-nc-nd/4.0

Cells were harvested and resuspended in the buffer containing 25 mM HEPES pH 7.4, 250 mM KCl, 5 μg/ml aprotinin, 1 μg/ml pepstatin, and 5 μg/ml leupeptin. The lysate was sonicated on ice. After high-speed centrifugation at 29,097 g for 1 h, the supernatant was loaded onto anti-FLAG M2 resin (Sigma). Then the resin was rinsed with wash buffer containing 25 mM HEPES pH 7.4, 250 mM KCl. Protein was eluted with wash buffer plus 0.4 mg/ml FLAG peptide. Elution was subjected to Superdex 200 Increase 10/300 GL column (GE Healthcare) in buffer containing 25 mM HEPES pH 7.4, 250 mM NaCl. Peak fractions were pooled for further experiments. Purified protein was dialyzed overnight against the buffer (5 mM HEPES pH 7.4) at 4°C to remove excess salts.

Actin was isolated from rabbit skeletal-muscle acetone powder[36] and further purified by gel filtration on Sephacryl S-300 in Ca-G buffer (2 mM imidazole pH 7.0, 0.2 mM ATP, 0.1 mM $CaCl_2$ and 0.5 mM dithiothreitol (DTT)). Pyrenyl-actin was produced by labelling Cys374 with pyrene iodoacetamide[37,38].

Recombinant *S. rosetta* and human actin were purified using a protocol adapted from a previously described method[39]. Actin-coding sequences (Human: ACTB, UniProt ID: P60709; *S. rosetta*, UniProt ID: F2U0P3) were cloned into pCAG vector, which adds, at the C-terminus, an in-frame chymotrypsin cleavage site, linker sequence, thymosin β4 and a His tag[40]. 2 mg plasmid and 4 mg polyethylenimine (YEASON) were preincubated in 50 ml fresh SMM 293-TII medium (Sino Biological) for 30 min before adding into one litre HEK293F cells at density of 2.0×10^6 cells per ml, and then incubate at 37 °C for 48 h under 5% CO_2. Cells were harvested and resuspended in 1× binding buffer [10 mM imidazole, 10 mM HEPES pH 7.4, 300 mM NaCl, 2mM $MgCl_2$, 1 mM ATP, 1 mM phenylmethylsulfonyl fluoride (PMSF), 7 mM β-mercaptoethanol (β-

Langtaosha (LTS) Preprint doi: https://doi.org/10.65215/LTSpreprints.2026.11.11.000383. This version posted November 11, 2026. The copyright holder for this preprint (which was not certified by peer review) is the author/funder. Creative Commons license: CC Attribution-NonCommercial-NoDerivatives 4.0 https://creativecommons.org/licenses/by-nc-nd/4.0

ME), 5 μg/ml aprotinin, 1 μg/ml pepstatin, and 5 μg/ml leupeptin]. The lysate was sonicated on ice.

After high-speed centrifugation at 29,097 g for 1 h, the supernatant was incubated with 1 ml nickel resin at 4°C for 1-1.5 h. The resin was pelleted down by centrifugation at 4°C at 1258 g for 5 min and washed with 25 ml ice-cold binding buffer composed of 10 mM imidazole, 10 mM HEPES pH 7.4, 300 mM NaCl, 2 mM $MgCl_2$, 1 mM ATP, 1 mM PMSF and 7 mM β-ME, 5 μg/ml aprotinin, 1 μg/ml pepstatin, and 5 μg/ml leupeptin. The resin was loaded into an open column and washed first with ice-cold 20 ml binding buffer, then with 45 ml ice-cold G-buffer composed of 5 mM HEPES (pH 7.4), 0.2 mM $CaCl_2$, 0.2 mM ATP and 0.5 mM dithiothreitol (DTT). The resin was resuspended in 6 ml ice-cold G-buffer containing 5 μg/ml TLCK-treated chymotrypsin (Aladdin, #C129079) and incubated overnight at 4°C. The chymotrypsin was inactivated by addition of PMSF to 1 mM and incubated for 30 min on ice. The eluate was then collected into a tube.

Actin retained on the resin was eluted with 12 ml G-buffer and all the elution fractions were combined. The eluate was concentrated using a 30 kDa cut-off membrane and the final volume adjusted to 900 μl with ice-cold G-buffer. Actin was polymerized by addition of 100 μl 10× MEK buffer, composed of 20 mM $MgCl_2$, 50 mM glycol-bis(2-aminoethylether)-N,N,N′, N′-tetraacetic (EGTA) and 1 M KCl, for 1 h at RT. F-actin was pelleted by ultracentrifugation for 1 h at RT at 45,000 rpm (Beckman TLA-55 rotor) and re-suspended in 1 ml ice cold G-buffer. F-actin was depolymerized by dialysis against 1 L G-buffer at 4°C for 2 days. Dialysis buffer was exchanged every 12 h. Any remaining F-actin was pelleted by ultracentrifugation at RT at 45,000

Langtaosha (LTS) Preprint doi: https://doi.org/10.65215/LTSpreprints.2026.11.11.000383. This version posted November 11, 2026. The copyright holder for this preprint (which was not certified by peer review) is the author/funder. Creative Commons license: CC Attribution-NonCommercial-NoDerivatives 4.0 https://creativecommons.org/licenses/by-nc-nd/4.0

rpm for 30 min (Beckman TLA-55 rotor) and actin in the supernatant was concentrated to 100 μM using a 30 kDa cut-off membrane.

Western blotting

Samples were denatured in loading buffer, resolved by SDS-PAGE, and transferred to PVDF membranes. Membranes were blocked in 5% milk, incubated overnight at 4 °C with primary anti-FLAG antibody (1:1000) (CWBIO), washed, and probed with HRP-conjugated secondary antibodies (1:10000) before ECL detection.

Low-speed F-actin co-sedimentation assay

The low-speed F-actin co-sedimentation assay was adapted from previously published methods[41]. Rabbit skeletal muscle actin was used in these assays. All proteins were pre-clarified at 20,000 g for 30 min at 4°C. Briefly, preassembled actin filaments (3 μM) were incubated with recombinant Lasp or truncations for 30 min at RT and centrifuged at low speed (13,600 g) for 30 min at 4°C. The protein samples in the supernatant and pellet fractions were separated by SDS-PAGE and revealed by staining with Coomassie Brilliant blue R 250. The amount of actin in the supernatant was quantified by densitometry using ImageJ software.

Pyrene-actin polymerization and depolymerization assays

These assays are performed as previously described with minor modifications[42]. Rabbit skeletal muscle actin was used in these assays.

Langtaosha (LTS) Preprint doi: https://doi.org/10.65215/LTSpreprints.2026.11.11.000383. This version posted November 11, 2026. The copyright holder for this preprint (which was not certified by peer review) is the author/funder. Creative Commons license: CC Attribution-NonCommercial-NoDerivatives 4.0 https://creativecommons.org/licenses/by-nc-nd/4.0

For polymerization assays, monomeric actin (G-actin) was mixed with pyrene-labeled G-actin at a 1:1 molar ratio to a final concentration of 5 μM (50% pyrene-G-actin). Immediately before polymerization, Ca-ATP-actin was converted to Mg-ATP-actin by incubation with one-tenth of a volume of 10 × ME buffer (2 mM EGTA and 0.5 mM $MgCl_2$) for 2 min on ice. Proteins were mixed on ice, and one-tenth of a volume of 10 × KMEI (500 mM KCl, 10 mM $MgCl_2$, 10 mM EGTA, 100 mM imidazole, pH 8.0) was added to initiate polymerization. Pyrene fluorescence of samples (200 μl) was monitored using a Photon Technologies International spectrofluorimeter with excitation at 365 nm and emission at 407 nm.

For depolymerization assays, preassembled pyrene-F-actin (5 μM final) was incubated with the indicated concentrations of test proteins in a total volume of 6 μL for 5 min at RT. Depolymerization was initiated by diluting the incubation mixture 25-fold into low-salt G-buffer composed of 5 mM HEPES (pH 7.4), 0.2 mM $CaCl_2$, 0.2 mM ATP and 0.5 mM DTT. The diluted samples were immediately transferred to a fluorometer cuvette. Pyrene fluorescence of samples (200 μl) was monitored using a Photon Technologies International spectrofluorimeter with excitation at 365 nm and emission at 407 nm.

Fluorescence data were processed using Microsoft Excel and analyzed using GraphPad Prism. For polymerization assays, the initial fluorescence intensities of all traces were aligned to that of the corresponding actin-alone control. The aligned traces were then baseline-subtracted and normalized to the initial fluorescence intensity of the actin-alone control, preserving differences in fluorescence amplitude among conditions. For comparison of relative polymerization kinetics, each trace was additionally subjected to min–max normalization by subtracting its minimum

Langtaosha (LTS) Preprint doi: https://doi.org/10.65215/LTSpreprints.2026.11.11.000383. This version posted November 11, 2026. The copyright holder for this preprint (which was not certified by peer review) is the author/funder. Creative Commons license: CC Attribution-NonCommercial-NoDerivatives 4.0 https://creativecommons.org/licenses/by-nc-nd/4.0

fluorescence intensity and dividing by the difference between its maximum and minimum intensities.

For depolymerization assays, the initial fluorescence intensities of all traces were similarly aligned to that of the corresponding actin-alone control. The aligned traces were then normalized by subtracting the endpoint fluorescence intensity of the actin-alone control and dividing by the difference between the initial and endpoint fluorescence intensities of that control. Apparent fluorescence decay rate constants (k) were determined by fitting the normalized traces to a single-exponential decay model using GraphPad Prism. For each independent experiment, the relative decay rate constant (k/k_0) was calculated by normalizing the fitted rate constant of each treatment to that of the corresponding actin-alone control (k_0).

When multiple technical measurements were performed within the same experiment, the fitted rate constants were averaged before calculating the relative decay rate constant. Data are presented as mean ± SEM where applicable, with one to four independent experiments per condition (n = 1–4). Error bars were omitted for conditions with only one independent experiment.

Direct visualization of individual actin filaments by fluorescence light microscopy or Cryo-EM

Recombinant *S. rosetta* and human actin were used in these assays. Immediately before polymerization, Ca-ATP-actin was converted to Mg-ATP-actin by incubation with one-tenth of a volume of 10 × ME buffer (2 mM EGTA and 0.5 mM $MgCl_2$) for 2 min on ice. Proteins were mixed on ice, and one-tenth of a volume of 10 × KMEH (1 M KCl, 20 mM $MgCl_2$, 10 mM EGTA,

Langtaosha (LTS) Preprint doi: https://doi.org/10.65215/LTSpreprints.2026.11.11.000383. This version posted November 11, 2026. The copyright holder for this preprint (which was not certified by peer review) is the author/funder. Creative Commons license: CC Attribution-NonCommercial-NoDerivatives 4.0 https://creativecommons.org/licenses/by-nc-nd/4.0

100 mM HEPES pH 7.5) was added to initiate polymerization and incubate at RT for 1 h, yielding 15 μM F-actin.

For bundling reactions, 3.4 μL of Lasp protein (various concentrations) was mixed with 2 μL of 15 μM F-actin and 0.6 μL 10× KMEH, followed by a 30-min incubation at RT. For fluorescence light microscopy, filaments were stained with phalloidin-488 (1:50 in 1× KMEH) for 30 min. And then, 2 μL aliquot was mounted on a glass slide and imaged on a Zeiss LSM980 Airyscan2 using a 60× oil objective. Images were processed in Imaris.

For Cryo-EM, 4 μL aliquots of the sample were applied to grids (Quantifoil Au R1.2/1.3, 300 mesh) glowdischarged for 30-35 s using the medium power setting of the Plasma Cleaner PDC32G (Harrick) and blotted for 3.0 s before being flash-frozen in liquid ethane cooled by liquid nitrogen with Vitrobot Mark IV (Thermo Fisher Scientific) at 8 °C and 100% humidity.

SPR experiments

SPR experiments were performed using a protocol adapted from a previously described BLI assay[43]. Rabbit skeletal muscle actin was used in these assays.

SPR experiments were conducted on a Biacore 8K+ system using streptavidin (SA) sensor chips (GE Healthcare). Prior to immobilization, the SA surface was preconditioned with sequential injections of 1 M NaCl / 50 mM NaOH to remove loosely bound contaminants. After immobilization, the chip was subjected to a stringent wash using 50% isopropanol / 1 M NaCl / 50 mM NaOH to eliminate hydrophobic or non-specific adsorbates and to stabilize the baseline. And then the surfaces were equilibrated in F-buffer [10 mM HEPES, pH 7.5, 50 mM KCl, 2 mM $MgCl_2$, 0.4mM ATP, 1 mM EGTA, 0.05% Tween-20 (v/v)] for 30 seconds. Firstly, biotinylated

Langtaosha (LTS) Preprint doi: https://doi.org/10.65215/LTSpreprints.2026.11.11.000383. This version posted November 11, 2026. The copyright holder for this preprint (which was not certified by peer review) is the author/funder. Creative Commons license: CC Attribution-NonCommercial-NoDerivatives 4.0 https://creativecommons.org/licenses/by-nc-nd/4.0

and nonbiotinylated G-actin were mixed in 1:4 ratio, diluted to final concentration of 5 μM. To minimize SPR signal artifacts caused by long actin filaments, 5 μM G-actin was polymerized in the presence of 0.5 μM gelsolin to generate short F-actin filaments. The filaments were immobilized on the SA sensor chip to an immobilization level of approximately 1,000 response units (RU).

For single-cycle kinetic measurements, analyte was injected over flow cells 1 and 2 at five increasing concentrations per cycle, with a contact time of 120 s and a dissociation time of 600 s at a flow rate of 30 μl/min. Buffer injections were included as startup cycles using a contact time of 120 s and a dissociation time of 60 s.

For multi-cycle kinetic measurements, analyte was injected over flow cells 1 and 2 at variable concentrations, with a contact time of 120 s and a dissociation time of 120 s at a flow rate of 30 μl/min. Between injections, the surface was treated with 1× F-buffer for 30 s at 30 μl/min. Sensorgrams were analyzed using Biacore S200 Evaluation Software, and binding affinities (K_d) derived from steady-state fitting of the equilibrium binding responses. All SPR experiments were independently repeated three times to ensure reproducibility and statistical reliability. Both kinetic (1:1 Langmuir) and steady-state affinity analyses were performed. Because immobilized F-actin filaments provide multiple binding sites and the interaction exhibits complex binding kinetics that may deviate from a simple 1:1 model, K_d values reported in this study were derived from steady-state affinity fitting.

Langtaosha (LTS) Preprint doi: https://doi.org/10.65215/LTSpreprints.2026.11.11.000383. This version posted November 11, 2026. The copyright holder for this preprint (which was not certified by peer review) is the author/funder. Creative Commons license: CC Attribution-NonCommercial-NoDerivatives 4.0 https://creativecommons.org/licenses/by-nc-nd/4.0

Cryo-EM data acquisition

Cryo-EM data were collected on a 300 kV Titan Krios G3i equipped with a Gatan K3 detector and a GIF Quantum energy filter (slit width of 20 eV). The defocus values ranged from −1.3 µm to −1.8 µm. Each stack of 32 frames was exposed for 2.56 s, and the exposure time of each frame was 0.08 s. The micrographs were automatically collected with the AutoEMation program[44] in super-resolution counting mode with a binned pixel size of 1.0742 Å. The total dose of each stack was about 50 e^{-} $Å^{-2}$. All 32 frames in each stack were aligned and summed using the whole-image motion correction program MotionCor2[45]. Contrast transfer function (CTF) parameters were estimated in cryoSPARC[46].

Cryo-ET data acquisition

Cryo-ET data were collected on a 300 kV Titan Krios G3i equipped with a Gatan K3 detector and a GIF Quantum energy filter (slit width of 20 eV). Virions were recorded in super-resolution mode in a calibrated pixel size of 1.6544 Å. Then, 150 sets of tilt-series data were collected using the dose-symmetric scheme [47] and 12 sets of tilt-series using bidirectional scheme from -60° to 60° at 3° steps and at various defocus between -3.0 and -5.0 µm in SerialEM[48]. At each tilt, a movie consisting of eight frames was recorded with 0.0265 s/frame exposure, giving a total dose of 123 $e^{-}/Å^{2}$ per tilt series (Table S1).

Cryo-EM data processing

For the *S. rosetta* microvilli dataset, an initial manual picking strategy was used to generate particle templates. A total of 3,651 particles were manually picked from representative micrographs using a box size of 1024 pixels and were subsequently cropped to 128 pixels, corresponding to a pixel

Langtaosha (LTS) Preprint doi: https://doi.org/10.65215/LTSpreprints.2026.11.11.000383. This version posted November 11, 2026. The copyright holder for this preprint (which was not certified by peer review) is the author/funder. Creative Commons license: CC Attribution-NonCommercial-NoDerivatives 4.0 https://creativecommons.org/licenses/by-nc-nd/4.0

size of 8.5936 Å. Two-dimensional (2D) class averages showing clear filamentous features were selected, and four representative class averages were used as templates for template-based particle picking. For full-dataset processing, 10,338 micrographs with a pixel size of 1.0742 Å were used. Template-based picking yielded 171,398,451 particles, which were extracted with a box size of 384 pixels and cropped to 128 pixels for binned processing. An initial heterogeneous refinement was performed using the binned particles, after which 2,222,767 particles were re-extracted with the remove of duplicated particles. A subset of 1,710,787 particles was retained for local refinement. Three-dimensional (3D) classification without alignment was then used to further sort particle populations, followed by final local refinement. The final reconstruction was obtained from 477,020 particles and reached a gold-standard FSC resolution of 3.16 Å. Local resolution estimation showed variable resolution across the reconstructed density, with the best-resolved regions reaching approximately 2.5-3.5 Å.

For the mouse skeletal thin filaments dataset, a similar initial picking workflow was used to generate a reliable reference for template based particle picking. 2,401,134 particles from 1,550 micrographs are initially extracted for 2D analysis. Particles were extracted using a box size of 400 pixels and rescaled to 128 pixels. After two rounds of 2D classification, 501,577 particles were selected for ab initio reconstruction. The most suitable reference was selected based on the presence of filamentous structural features. The selected particles were subjected to heterogeneous refinement and duplicate particle removal, yielding 342,624 particles. Subsequent non-uniform refinement produced a map in which the main filament density was visible but nebulin density was not clearly resolved. A focused mask was therefore generated around the region of interest, and 3D classification was performed to identify particles containing additional nebulin-like density. This classification yielded 23,406 particles with detectable nebulin density, which were used as a

Langtaosha (LTS) Preprint doi: https://doi.org/10.65215/LTSpreprints.2026.11.11.000383. This version posted November 11, 2026. The copyright holder for this preprint (which was not certified by peer review) is the author/funder. Creative Commons license: CC Attribution-NonCommercial-NoDerivatives 4.0 https://creativecommons.org/licenses/by-nc-nd/4.0

reference for full dataset processing. For full-dataset processing, 2,469 micrographs with a pixel size of 1.0825 Å were processed using Topaz-based particle extraction[49]. Topaz picking yielded 3,235,155 particles, which were extracted with a box size of 256 pixels and rescaled to 128 pixels. After 2D classification, 1,250,214 particles were retained and subjected to heterogeneous refinement. A refined subset of 832,295 particles was further processed by 3D classification, duplicate removal, non-uniform refinement, and local refinement. The final reconstruction was generated from 103,394 particles and reached a gold-standard FSC resolution of 2.98 Å. Local resolution analysis indicated that the central core of the reconstruction was better resolved than peripheral regions, with local resolution values ranging approximately from 2.5 to 4.5 Å.

Cryo-ET data processing

An initial subset of 14 tilt series was used to establish the processing pipeline and model trainning for automated particle picking. Movie frames from tilt series were motion-corrected, and contrast transfer function (CTF) parameters were estimated in Warp[50]. The tilt series were then automatically aligned and reconstructed using AreTomo[51]. For initial particle identification, 2,124 particles were manually picked from reconstructed tomograms. These manually picked particles were used both to train a cryoYOLO model for auto-picking and to extract pseudo-subtomograms for initial volume generation[52]. The initial reconstruction generated from the manually picked particles showed clear actin bundle densities and was used as a reference for subsequent classification and refinement.

After establishing the initial workflow, a total of 37 tilt series were processed. All tilt series were preprocessed in the same way described above. Automated particle picking was performed

Langtaosha (LTS) Preprint doi: https://doi.org/10.65215/LTSpreprints.2026.11.11.000383. This version posted November 11, 2026. The copyright holder for this preprint (which was not certified by peer review) is the author/funder. Creative Commons license: CC Attribution-NonCommercial-NoDerivatives 4.0 https://creativecommons.org/licenses/by-nc-nd/4.0

using the trained cryoYOLO model, resulting in 32,315 particles. Particles were initially extracted at a pixel size of 6 Å with a box size of 128 pixels and subjected to two rounds of 3D classification with global search by RELION[53]. 8,522 subtomograms were kept to re-extract at a pixel size of 4 Å. A focused mask was generated around the seven F-actin lattice core. Masked 3D classification with local search was performed yielding a final resolution of approximately 13 Å with clear actin and fasin densities.

Cryo-EM data processing of F-actin bundles

11,470,105 particles from 9,650 micrographs were extracted with a box size of 640 pixels and a crop size of 120 pixels. The 13 Å cryo-ET reconstruction map was then used as a good reference for heterogeneous refinement. The resulting 2,273,308 particles were re-extracted with a box size of 640 pixels and a crop size of 240 pixels and subjected to 3D classification without alignment. A selected subset of 478,013 particles was further re-extracted with a box size of 640 pixels and a crop size of 480 pixels and subjected to an additional round of 3D classification without alignment. The final reconstruction, obtained from 226,105 particles, reached an overall resolution of 4.36 Å, as determined by the gold-standard Fourier shell correlation (FSC) 0.143 criterion

Finally, the final selected particles were re-extracted using a box size of 1,280 pixels and a crop size of 480 pixels, yielding a total of 171,503 particles. The reconstruction yielded an overall resolution of 5.79 Å.

Langtaosha (LTS) Preprint doi: https://doi.org/10.65215/LTSpreprints.2026.11.11.000383. This version posted November 11, 2026. The copyright holder for this preprint (which was not certified by peer review) is the author/funder. Creative Commons license: CC Attribution-NonCommercial-NoDerivatives 4.0 https://creativecommons.org/licenses/by-nc-nd/4.0

3D classification of microvillar actin bundle architectures

Following refinement of 171,503 particles extracted with a box size of 1,280 pixels, we obtained a reconstruction of the microvillar actin bundle at 5.79 Å resolution. The reconstruction revealed a central hexagonal arrangement of seven F-actin filaments (6+1), while additional peripheral filaments became visible at lower contour levels, although their densities were poorly resolved. To resolve this structural heterogeneity, two focus masks were generated to encompass the central actin core and the surrounding outer shell, respectively.

Using the outer-shell mask, the 171,503 particles were subjected to two independent rounds of 3D classification into five and six classes, respectively. Both classifications identified two distinct bundle architectures: one containing seven membrane-enclosed actin filaments and another containing an additional outer ring of 12 actin filaments within the membrane. For the seven-filament architecture, 52,593 and 60,307 particles were selected from the two classifications, respectively. These particles were combined, and duplicates were removed, yielding 69,187 particles for local refinement. Similarly, 37,243 and 41,618 particles corresponding to the 19-filament architecture were combined and deduplicated, resulting in 47,133 particles for local refinement.

The resulting locally refined maps were then used as initial volumes for further 3D classification with the outer-shell mask. Following particle selection and final local refinement, 39,482 particles contributed to the seven-filament reconstruction, while 42,584 particles contributed to the 19-filament reconstruction. The final reconstructions reached overall resolutions of 7.42 Å and 7.44 Å, respectively, as determined by the gold-standard Fourier shell correlation (FSC) 0.143 criterion.

Langtaosha (LTS) Preprint doi: https://doi.org/10.65215/LTSpreprints.2026.11.11.000383. This version posted November 11, 2026. The copyright holder for this preprint (which was not certified by peer review) is the author/funder. Creative Commons license: CC Attribution-NonCommercial-NoDerivatives 4.0 https://creativecommons.org/licenses/by-nc-nd/4.0

Model building and refinement

The initial *Sr*Lasp and actin structure model was derived using AlphaFold2[54]. The predicted model was fitted into the cryo-EM map of *S. rosetta* F-actin by UCSF ChimeraX[55]. Coot was used for manual adjustment and rebuilding of the structure[56]. Coot was also used for manual adjustment and rebuilding of the mouse actin and nebulin structure. The consensus sequence of mouse Nebulin was used for model building. The final models of all datasets were refined against the corresponding maps using PHENIX in real space with secondary structure and geometry restraints[57]. The structures were validated through examination of the Clash scores, Molprobity scores and statistics of the Ramachandran plots by PHENIX (Table S2).

Phylogenetic analysis

To investigate the evolutionary relationships of Nebulin-family proteins, representative metazoan and filozoan species were first surveyed together with representative non-filozoan lineages to assess the phylogenetic distribution of Nebulin-family homologs (Figure S4A). Protein sequences were retrieved from UniProtKB based on sequence similarity and domain organization. Representative LASP proteins (n = 37) and Nebulin/Nebulette/N-RAP proteins (n = 24) were analyzed separately.

Because LASP proteins are considerably shorter and contain only several Nebulin repeats, whereas Nebulin, Nebulette, and N-RAP contain extensive tandem Nebulin-repeat arrays, phylogenetic analyses were performed separately for the LASP subfamily and the

Langtaosha (LTS) Preprint doi: https://doi.org/10.65215/LTSpreprints.2026.11.11.000383. This version posted November 11, 2026. The copyright holder for this preprint (which was not certified by peer review) is the author/funder. Creative Commons license: CC Attribution-NonCommercial-NoDerivatives 4.0 https://creativecommons.org/licenses/by-nc-nd/4.0

Nebulin/Nebulette/N-RAP subfamily to avoid artifacts resulting from extreme differences in protein length and domain composition.

Protein sequences within each group were subjected to multiple sequence alignment using MUSCLE[58] implemented in the One Step Build a ML Tree workflow of TBtools-II (v2.337)[59]. Poorly aligned regions were automatically trimmed using trimAl[60]. Maximum-likelihood phylogenetic trees were inferred using IQ-TREE v1.6.12[61] with automatic model selection by ModelFinder. For the LASP dataset, the best-fitting amino acid substitution model was LG+G4, whereas the Nebulin/Nebulette/N-RAP dataset was best described by LG+I+G4, according to the Bayesian Information Criterion (BIC). Branch support was estimated using 5,000 ultrafast bootstrap replicates with branch-length optimization. The resulting Newick-format trees were imported into iTOL (Interactive Tree of Life)[62] for visualization, annotation, and integration of protein domain architectures.

Scanning electron microscopy (SEM)

For SEM analysis of glutaraldehyde-fixed *S. rosetta*, approximately 4×10^6 cells were collected and resuspended in fixation buffer containing 2% glutaraldehyde in artificial seawater (ASW). Fixed cells were washed four times with 0.1 M phosphate buffer (PB; 15 min per wash) and subsequently post-fixed with 1% osmium tetroxide (OsO_4) for 1 h. Samples were rinsed with buffer and dehydrated through a graded ethanol series (50%, 70%, 80%, and 90% ethanol once each, followed by 100% ethanol three times; 5 min per step). The dehydrated samples were subjected to critical point drying.

Langtaosha (LTS) Preprint doi: https://doi.org/10.65215/LTSpreprints.2026.11.11.000383. This version posted November 11, 2026. The copyright holder for this preprint (which was not certified by peer review) is the author/funder. Creative Commons license: CC Attribution-NonCommercial-NoDerivatives 4.0 https://creativecommons.org/licenses/by-nc-nd/4.0

Dried samples were mounted onto aluminum SEM stubs using double-sided conductive carbon tape. A small amount of dried cell samples were transferred onto the tape using a clean toothpick and gently dispersed onto the stub surface. Samples were coated with gold using a sputter coater (Hitachi ES-1010) at 15 mA for 60 s, resulting in an approximate coating thickness of 10 nm. SEM imaging was performed at room temperature (RT) using a FEI Helios NanoLab G3 UC system (serial no. 9922567) operated at an accelerating voltage of 2 kV. Images were acquired at a magnification of 10,000×.

SUPPLEMENTAL INFORMATION

ACKNOWLEDGMENTS

We thank Prof. Nicole King, Becca Arruda and Michael David Carver (UC Berkeley) for providing *S. rosetta* and culture guidance. We thank Prof. Shanjin Huang (Tsinghua University) for his guidance on actin-related experiments. We thank Dr. Fan Yang and Dr. Niyun Zhou from Technology Center of Protein Research at Tsinghua University for their technical support during EM data collection. We thank Dr. Xiaomin Li and Dr. Ying Li from the Technology Center of Protein Research, and Chenguang Zhao and Qian Li from the Center of Biomedical Analysis at Tsinghua University, for their technical assistance with SEM. We thank the Tsinghua University Branch of China National Center for Protein Sciences (Beijing) for providing the cryo-EM facility support and the computational facility support.

Funding

Langtaosha (LTS) Preprint doi: https://doi.org/10.65215/LTSpreprints.2026.11.11.000383. This version posted November 11, 2026. The copyright holder for this preprint (which was not certified by peer review) is the author/funder. Creative Commons license: CC Attribution-NonCommercial-NoDerivatives 4.0 https://creativecommons.org/licenses/by-nc-nd/4.0

This work was funded by the National Natural Science Foundation of China (32341016, C.Y), Tsinghua-Peking University Center for Life Sciences (20111770319, C.Y) and the Tsinghua University Initiative Scientific Research Program (20241080049, 20251080093, C.Y), Beijing Frontier Research Center for Biological Structure, State Key Laboratory of Membrane Biology, Tsinghua University Initiative Scientific Research Program, and Start-up funds from Tsinghua-Peking Center for Life Sciences and Tsinghua University.

AUTHOR CONTRIBUTIONS

C.Y. conceived the project. S.Z., J.T., Y.S., and C.Y. designed all experiments. S.Z., Y.S., and T.Z. performed the experiments. F.K., S.Z., and C.Y. contributed to the structural determination. S.Z., F.K., J.T., Y.S., S. H., and C.Y. analyzed the data and contributed to manuscript preparation. S.Z. and C.Y. wrote the manuscript.

DECLARATION OF INTERESTS

Authors declare that they have no competing interests.

REFERENCES

1. Lawson, C.D., and Ridley, A.J. (2017). Rho GTPase signaling complexes in cell migration and invasion. Journal of Cell Biology *217*, 447-457. https://doi.org/10.1083/jcb.201612069.
2. Machesky, L.M. (2008). Lamellipodia and filopodia in metastasis and invasion. FEBS Lett *582*, 2102-2111. https://doi.org/10.1016/j.febslet.2008.03.039.
3. Paz, H., Pathak, N., and Yang, J. (2014). Invading one step at a time: the role of invadopodia in tumor metastasis. Oncogene *33*, 4193-4202. https://doi.org/10.1038/onc.2013.393.
4. Ansel, M., Ramachandran, K., Dey, G., and Brunet, T. (2024). Origin and evolution of microvilli. Biol Cell *116*, e2400054. https://doi.org/10.1111/boc.202400054.
5. Meenderink, L.M., Gaeta, I.M., Postema, M.M., Cencer, C.S., Chinowsky, C.R., Krystofiak, E.S., Millis, B.A., and Tyska, M.J. (2019). Actin Dynamics Drive Microvillar Motility and Clustering during Brush Border Assembly. Dev Cell *50*, 545-556.e544. https://doi.org/10.1016/j.devcel.2019.07.008.

Langtaosha (LTS) Preprint doi: https://doi.org/10.65215/LTSpreprints.2026.11.11.000383. This version posted November 11, 2026. The copyright holder for this preprint (which was not certified by peer review) is the author/funder. Creative Commons license: CC Attribution-NonCommercial-NoDerivatives 4.0 https://creativecommons.org/licenses/by-nc-nd/4.0

6. Bretscher, A., and Weber, K. (1978). Purification of microvilli and an analysis of the protein components of the microfilament core bundle. Exp Cell Res *116*, 397-407. https://doi.org/10.1016/0014-4827(78)90463-9.
7. Zhu, H., Li, M., Zhao, R., Li, M., Chai, Y., Zhu, Z., Yang, Y., Li, W., Xie, Z., Li, X., et al. (2022). In situ structure of intestinal apical surface reveals nanobristles on microvilli. Proc Natl Acad Sci U S A *119*, e2122249119. https://doi.org/10.1073/pnas.2122249119.
8. Brown, J.W., and McKnight, C.J. (2010). Molecular model of the microvillar cytoskeleton and organization of the brush border. PLoS One *5*, e9406. https://doi.org/10.1371/journal.pone.0009406.
9. Ho, C.M., Li, X., Lai, M., Terwilliger, T.C., Beck, J.R., Wohlschlegel, J., Goldberg, D.E., Fitzpatrick, A.W.P., and Zhou, Z.H. (2020). Bottom-up structural proteomics: cryoEM of protein complexes enriched from the cellular milieu. Nat Methods *17*, 79-85. https://doi.org/10.1038/s41592-019-0637-y.
10. Liu, S., Xia, X., Calvo, E., and Zhou, Z.H. (2023). Native structure of mosquito salivary protein uncovers domains relevant to pathogen transmission. Nat Commun *14*, 899. https://doi.org/10.1038/s41467-023-36577-y.
11. Wang, C., Jiang, W., Leitz, J., Yang, K., Esquivies, L., Wang, X., Shen, X., Held, R.G., Adams, D.J., Basta, T., et al. (2024). Structure and topography of the synaptic V-ATPase-synaptophysin complex. Nature *631*, 899-904. https://doi.org/10.1038/s41586-024-07610-x.
12. Sebé-Pedrós, A., Burkhardt, P., Sánchez-Pons, N., Fairclough, S.R., Lang, B.F., King, N., and Ruiz-Trillo, I. (2013). Insights into the origin of metazoan filopodia and microvilli. Mol Biol Evol *30*, 2013-2023. https://doi.org/10.1093/molbev/mst110.
13. Zettler, L.A.A., Nerad, T.A., O'Kelly, C.J., and Sogin, M.L. (2001). The nucleariid amoebae: more protists at the animal-fungal boundary. J Eukaryot Microbiol *48*, 293-297. https://doi.org/10.1111/j.1550-7408.2001.tb00317.x.
14. Mylnikov, A.P., Tikhonenkov, D.V., Karpov, S.A., and Wylezich, C. (2019). Microscopical Studies on Ministeria vibrans Tong, 1997 (Filasterea) Highlight the Cytoskeletal Structure of the Common Ancestor of Filasterea, Metazoa and Choanoflagellata. Protist *170*, 385-396. https://doi.org/10.1016/j.protis.2019.07.001.
15. Shalchian-Tabrizi, K., Minge, M.A., Espelund, M., Orr, R., Ruden, T., Jakobsen, K.S., and Cavalier-Smith, T. (2008). Multigene phylogeny of choanozoa and the origin of animals. PLoS One *3*, e2098. https://doi.org/10.1371/journal.pone.0002098.
16. Brunet, T., and King, N. (2017). The Origin of Animal Multicellularity and Cell Differentiation. Dev Cell *43*, 124-140. https://doi.org/10.1016/j.devcel.2017.09.016.
17. Dayel, M.J., and King, N. (2014). Prey capture and phagocytosis in the choanoflagellate Salpingoeca rosetta. PLoS One *9*, e95577. https://doi.org/10.1371/journal.pone.0095577.
18. Pappas, C.T., Krieg, P.A., and Gregorio, C.C. (2010). Nebulin regulates actin filament lengths by a stabilization mechanism. J Cell Biol *189*, 859-870. https://doi.org/10.1083/jcb.201001043.
19. Wang, Z., Grange, M., Pospich, S., Wagner, T., Kho, A.L., Gautel, M., and Raunser, S. (2022). Structures from intact myofibrils reveal mechanism of thin filament regulation through nebulin. Science *375*, eabn1934. https://doi.org/10.1126/science.abn1934.
20. Pappas, C.T., Bliss, K.T., Zieseniss, A., and Gregorio, C.C. (2011). The Nebulin family: an actin support group. Trends Cell Biol *21*, 29-37. https://doi.org/10.1016/j.tcb.2010.09.005.
21. Fujita, Y., Chokki, T., Nishioka, T., Morimoto, K., Nakayama, A., Nakae, H., Ogasawara, M., and Terasaki, A.G. (2021). The emergence of nebulin repeats and

Langtaosha (LTS) Preprint doi: https://doi.org/10.65215/LTSpreprints.2026.11.11.000383. This version posted November 11, 2026. The copyright holder for this preprint (which was not certified by peer review) is the author/funder. Creative Commons license: CC Attribution-NonCommercial-NoDerivatives 4.0 https://creativecommons.org/licenses/by-nc-nd/4.0

evolution of lasp family proteins. Cytoskeleton (Hoboken) *78*, 419-435. https://doi.org/10.1002/cm.21693.

22. Fernandes, I., and Schöck, F. (2014). The nebulin repeat protein Lasp regulates I-band architecture and filament spacing in myofibrils. J Cell Biol *206*, 559-572. 10.1083/jcb.201401094.
23. Huang, S., Robinson, R.C., Gao, L.Y., Matsumoto, T., Brunet, A., Blanchoin, L., and Staiger, C.J. (2005). Arabidopsis VILLIN1 generates actin filament cables that are resistant to depolymerization. Plant Cell *17*, 486-501. https://doi.org/10.1105/tpc.104.028555.
24. Holmes, K.C., Popp, D., Gebhard, W., and Kabsch, W. (1990). Atomic model of the actin filament. Nature *347*, 44-49. https://doi.org/10.1038/347044a0.
25. Reynolds, M.J., Hachicho, C., Carl, A.G., Gong, R., and Alushin, G.M. (2022). Bending forces and nucleotide state jointly regulate F-actin structure. Nature *611*, 380-386. https://doi.org/10.1038/s41586-022-05366-w.
26. Gong, R., Reynolds, M.J., Carney, K.R., Hamilton, K., Bidone, T.C., and Alushin, G.M. (2025). Fascin structural plasticity mediates flexible actin bundle construction. Nat Struct Mol Biol *32*, 940-952. https://doi.org/10.1038/s41594-024-01477-2.
27. Richter, D.J., Fozouni, P., Eisen, M.B., and King, N. (2018). Gene family innovation, conservation and loss on the animal stem lineage. Elife *7*. https://doi.org/10.7554/eLife.34226.
28. Banjade, S., Wu, Q., Mittal, A., Peeples, W.B., Pappu, R.V., and Rosen, M.K. (2015). Conserved interdomain linker promotes phase separation of the multivalent adaptor protein Nck. Proc Natl Acad Sci U S A *112*, E6426-6435. https://doi.org/10.1073/pnas.1508778112.
29. Saksela, K., and Permi, P. (2012). SH3 domain ligand binding: What's the consensus and where's the specificity? FEBS Lett *586*, 2609-2614. https://doi.org/10.1016/j.febslet.2012.04.042.
30. Zieseniss, A., Terasaki, A.G., and Gregorio, C.C. (2008). Lasp-2 expression, localization, and ligand interactions: a new Z-disc scaffolding protein. Cell Motil Cytoskeleton *65*, 59-72. https://doi.org/10.1002/cm.20244.
31. Sauvanet, C., Wayt, J., Pelaseyed, T., and Bretscher, A. (2015). Structure, Regulation, and Functional Diversity of Microvilli on the Apical Domain of Epithelial Cells. Annual Review of Cell and Developmental Biology *31*, 593-621. https://doi.org/10.1146/annurev-cellbio-100814-125234.
32. Mattila, P.K., and Lappalainen, P. (2008). Filopodia: molecular architecture and cellular functions. Nature Reviews Molecular Cell Biology *9*, 446-454. https://doi.org/10.1038/nrm2406.
33. Tomasetto, C., Moog-Lutz, C., Régnier, C.H., Schreiber, V., Basset, P., and Rio, M.C. (1995). Lasp-1 (MLN 50) defines a new LIM protein subfamily characterized by the association of LIM and SH3 domains. FEBS Lett *373*, 245-249. https://doi.org/10.1016/0014-5793(95)01040-l.
34. Butt, E., Howard, C.M., and Raman, D. (2022). LASP1 in Cellular Signaling and Gene Expression: More than Just a Cytoskeletal Regulator. Cells *11*. https://doi.org/10.3390/cells11233817.
35. Levin, Tera C., and King, N. (2013). Evidence for Sex and Recombination in the Choanoflagellate Salpingoeca rosetta. Current Biology *23*, 2176-2180. https://doi.org/10.1016/j.cub.2013.08.061.

Langtaosha (LTS) Preprint doi: https://doi.org/10.65215/LTSpreprints.2026.11.11.000383. This version posted November 11, 2026. The copyright holder for this preprint (which was not certified by peer review) is the author/funder. Creative Commons license: CC Attribution-NonCommercial-NoDerivatives 4.0 https://creativecommons.org/licenses/by-nc-nd/4.0

36. Spudich, J.A., and Watt, S. (1971). The regulation of rabbit skeletal muscle contraction. I. Biochemical studies of the interaction of the tropomyosin-troponin complex with actin and the proteolytic fragments of myosin. J Biol Chem *246*, 4866-4871. https://doi.org/10.1016/S0021-9258(18)62016-2.
37. Kouyama, T., and Mihashi, K. (1981). Fluorimetry study of N-(1-pyrenyl) iodoacetamide-labelled F-actin: local structural change of actin protomer both on polymerization and on binding of heavy meromyosin. European Journal of Biochemistry *114*, 33-38. https://doi.org/10.1111/j.1432-1033.1981.tb06167.x.
38. Pollard, T.D. (1984). Polymerization of ADP-actin. J Cell Biol *99*, 769-777. https://doi.org/10.1083/jcb.99.3.769.
39. Hatano, T., Alioto, S., Roscioli, E., Palani, S., Clarke, S.T., Kamnev, A., Hernandez-Fernaud, J.R., Sivashanmugam, L., Chapa, Y.L.B., Jones, A.M.E., et al. (2018). Rapid production of pure recombinant actin isoforms in Pichia pastoris. J Cell Sci *131*. https://doi.org/10.1242/jcs.213827.
40. Noguchi, T.Q.P., Kanzaki, N., Ueno, H., Hirose, K., and Uyeda, T.Q.P. (2007). A Novel System for Expressing Toxic Actin Mutants in Dictyostelium and Purification and Characterization of a Dominant Lethal Yeast Actin Mutant*. Journal of Biological Chemistry *282*, 27721-27727. https://doi.org/10.1074/jbc.M703165200.
41. Kovar, D.R., Staiger, C.J., Weaver, E.A., and McCurdy, D.W. (2000). AtFim1 is an actin filament crosslinking protein from Arabidopsis thaliana. The Plant Journal *24*, 625-636. https://doi.org/10.1046/j.1365-313x.2000.00907.x.
42. Amann, K.J., and Pollard, T.D. (2001). The Arp2/3 complex nucleates actin filament branches from the sides of pre-existing filaments. Nature Cell Biology *3*, 306-310. https://doi.org/10.1038/35060104.
43. Hanč, P., Fujii, T., Iborra, S., Yamada, Y., Huotari, J., Schulz, O., Ahrens, S., Kjær, S., Way, M., Sancho, D., et al. (2015). Structure of the Complex of F-Actin and DNGR-1, a C-Type Lectin Receptor Involved in Dendritic Cell Cross-Presentation of Dead Cell-Associated Antigens. Immunity *42*, 839-849. https://doi.org/10.1016/j.immuni.2015.04.009.
44. Lei, J., and Frank, J. (2005). Automated acquisition of cryo-electron micrographs for single particle reconstruction on an FEI Tecnai electron microscope. J Struct Biol *150*, 69-80. https://doi.org/10.1016/j.jsb.2005.01.002.
45. Zheng, S.Q., Palovcak, E., Armache, J.P., Verba, K.A., Cheng, Y., and Agard, D.A. (2017). MotionCor2: anisotropic correction of beam-induced motion for improved cryo-electron microscopy. Nat Methods *14*, 331-332. https://doi.org/10.1038/nmeth.4193.
46. Punjani, A., Rubinstein, J.L., Fleet, D.J., and Brubaker, M.A. (2017). cryoSPARC: algorithms for rapid unsupervised cryo-EM structure determination. Nat Methods *14*, 290-296. https://doi.org/10.1038/nmeth.4169.
47. Hagen, W.J.H., Wan, W., and Briggs, J.A.G. (2017). Implementation of a cryo-electron tomography tilt-scheme optimized for high resolution subtomogram averaging. J Struct Biol *197*, 191-198. https://doi.org/10.1016/j.jsb.2016.06.007.
48. Mastronarde, D.N. (2005). Automated electron microscope tomography using robust prediction of specimen movements. J Struct Biol *152*, 36-51. https://doi.org/10.1016/j.jsb.2005.07.007.
49. Bepler, T., Morin, A., Rapp, M., Brasch, J., Shapiro, L., Noble, A.J., and Berger, B. (2019). Positive-unlabeled convolutional neural networks for particle picking in cryo-electron micrographs. Nat Methods *16*, 1153-1160. https://doi.org/10.1038/s41592-019-0575-8.

Langtaosha (LTS) Preprint doi: https://doi.org/10.65215/LTSpreprints.2026.11.11.000383. This version posted November 11, 2026. The copyright holder for this preprint (which was not certified by peer review) is the author/funder. Creative Commons license: CC Attribution-NonCommercial-NoDerivatives 4.0 https://creativecommons.org/licenses/by-nc-nd/4.0

50. Tegunov, D., and Cramer, P. (2019). Real-time cryo-electron microscopy data preprocessing with Warp. Nature Methods *16*, 1146-1152. https://doi.org/10.1038/s41592-019-0580-y.
51. Zheng, S., Wolff, G., Greenan, G., Chen, Z., Faas, F.G.A., Bárcena, M., Koster, A.J., Cheng, Y., and Agard, D.A. (2022). AreTomo: An integrated software package for automated marker-free, motion-corrected cryo-electron tomographic alignment and reconstruction. J Struct Biol X *6*, 100068. https://doi.org/10.1016/j.yjsbx.2022.100068.
52. Wagner, T., Merino, F., Stabrin, M., Moriya, T., Antoni, C., Apelbaum, A., Hagel, P., Sitsel, O., Raisch, T., Prumbaum, D., et al. (2019). SPHIRE-crYOLO is a fast and accurate fully automated particle picker for cryo-EM. Commun Biol *2*, 218. https://doi.org/10.1038/s42003-019-0437-z.
53. Burt, A., Toader, B., Warshamanage, R., von Kügelgen, A., Pyle, E., Zivanov, J., Kimanius, D., Bharat, T.A.M., and Scheres, S.H.W. (2024). An image processing pipeline for electron cryo-tomography in RELION-5. FEBS Open Bio *14*, 1788-1804. https://doi.org/10.1002/2211-5463.13873.
54. Jumper, J., Evans, R., Pritzel, A., Green, T., Figurnov, M., Ronneberger, O., Tunyasuvunakool, K., Bates, R., Žídek, A., Potapenko, A., et al. (2021). Highly accurate protein structure prediction with AlphaFold. Nature *596*, 583-589. https://doi.org/10.1038/s41586-021-03819-2.
55. Pettersen, E.F., Goddard, T.D., Huang, C.C., Meng, E.C., Couch, G.S., Croll, T.I., Morris, J.H., and Ferrin, T.E. (2021). UCSF ChimeraX: Structure visualization for researchers, educators, and developers. Protein Sci *30*, 70-82. https://doi.org/10.1002/pro.3943.
56. Emsley, P., and Cowtan, K. (2004). Coot: model-building tools for molecular graphics. Acta Crystallogr D Biol Crystallogr *60*, 2126-2132. https://doi.org/10.1107/s0907444904019158.
57. Afonine, P.V., Poon, B.K., Read, R.J., Sobolev, O.V., Terwilliger, T.C., Urzhumtsev, A., and Adams, P.D. (2018). Real-space refinement in PHENIX for cryo-EM and crystallography. Acta Crystallogr D Struct Biol *74*, 531-544. https://doi.org/10.1107/s2059798318006551.
58. Edgar, R.C. (2022). Muscle5: High-accuracy alignment ensembles enable unbiased assessments of sequence homology and phylogeny. Nat Commun *13*, 6968. https://doi.org/10.1038/s41467-022-34630-w.
59. Chen, C., Wu, Y., Li, J., Wang, X., Zeng, Z., Xu, J., Liu, Y., Feng, J., Chen, H., He, Y., and Xia, R. (2023). TBtools-II: A “one for all, all for one” bioinformatics platform for biological big-data mining. Molecular Plant *16*, 1733-1742. https://doi.org/10.1016/j.molp.2023.09.010.
60. Capella-Gutiérrez, S., Silla-Martínez, J.M., and Gabaldón, T. (2009). trimAl: a tool for automated alignment trimming in large-scale phylogenetic analyses. Bioinformatics *25*, 1972-1973. https://doi.org/10.1093/bioinformatics/btp348.
61. Minh, B.Q., Schmidt, H.A., Chernomor, O., Schrempf, D., Woodhams, M.D., von Haeseler, A., and Lanfear, R. (2020). IQ-TREE 2: New Models and Efficient Methods for Phylogenetic Inference in the Genomic Era. Mol Biol Evol *37*, 1530-1534. https://doi.org/10.1093/molbev/msaa015.
62. Letunic, I., and Bork, P. (2024). Interactive Tree of Life (iTOL) v6: recent updates to the phylogenetic tree display and annotation tool. Nucleic Acids Research *52*, W78-W82. https://doi.org/10.1093/nar/gkae268.

Langtaosha (LTS) Preprint doi: https://doi.org/10.65215/LTSpreprints.2026.11.11.000383. This version posted November 11, 2026. The copyright holder for this preprint (which was not certified by peer review) is the author/funder. Creative Commons license: CC Attribution-NonCommercial-NoDerivatives 4.0 https://creativecommons.org/licenses/by-nc-nd/4.0